Comparative verification of hydro-mechanical fracture behavior: Task G of international research project DECOVALEX–2023

Mostafa Mollaali[a], Olaf Kolditz[a,l], Mengsu Hu[b], Chan–Hee Park[c], Jung–Wook Park[c], Christopher McDermott[d], Neil Chittenden[e], Alex Bond[f], Jeoung Seok Yoon[g], Jian Zhou[h], Peng–Zhi Pan[i,o], Hejuan Liu[i,o], Wenbo Hou[i,o], Hongwu Lei[i,o], Liwei Zhang[i,o], Thomas Nagel[j], Markus Barsch[j], Wenqing Wang[a], Son Nguyen[k], Saeha Kwon[n], Changsoo Lee[n] and Keita Yoshioka[a,m,*]

[a]*Department of Environmental Informatics, Helmholtz Centre for Environmental Research–UFZ, Leipzig 04318, Germany*
[b]*Energy Geosciences Division, Lawrence Berkeley National Laboratory, Berkeley CA 94720, United States of America*
[c]*Deep Subsurface Storage and Disposal Research Center, Korea Institute of Geoscience and Mineral Resources (KIGAM), Daejeon 34132, Korea*
[d]*School of Geosciences, The University of Edinburgh, Edinburgh EH9 3FE, United Kingdom*
[e]*Quintessa Ltd, Henley-on-Thames RG9 1HG, United Kingdom*
[f]*Quintessa Ltd, Warrington WA3 7QU, United Kingdom*
[g]*DynaFrax UG (Limited), Potsdam 14467, Germany*
[h]*College of Architecture and Civil Engineering, Beijing University of Technology, China*
[i]*State Key Laboratory of Geomechanics and Geotechnical Engineering, Institute of Rock and Soil Mechanics, Chinese Academy of Sciences, Wuhan 430071, China*
[o]*University of Chinese Academy of Sciences, Beijing 100049, China*
[j]*Chair of Soil Mechanics and Foundation Engineering, Geotechnical Institute, Technische Universität Bergakademie Freiberg, Freiberg 26545, Germany*
[l]*Applied Environmental Systems Analysis, Technische Universität Dresden, Dresden 01069, Germany*
[k]*Environmental Risk Assessment Division, Canadian Nuclear Safety Commission, Ottawa ON K1P 5S9, Canada*
[m]*Department of Civil Engineering, University of Manitoba, Winnipeg MB R3T 5V6, Canada*
[n]*Korea Atomic Energy Research Institute, Daejeon 34057, Korea*

ABSTRACT

Numerical simulations become a necessity when experimental approaches cannot cover the required physical and time scale of interest. One of such area is a simulation of long-term host rock behaviors for nuclear waste disposal and simulation tools involved in the assessment must go through rigorous validation tests. The DECOVALEX project (Development of COupled models and their VAlidation against EXperiments) is dedicated to this purpose by international participants[1]. This work is part of the ongoing phase DECOVALEX–2023 (D–2023, Task G) particularly aiming to simulate fracture behaviors under various conditions. Here, we cross-verified a variety of numerical methods including continuous and discontinuous approaches against four benchmark exercises with emphasis on numerical accuracy and parameterization of the various numerical approaches. The systematic inter-comparisons of test cases highlight advantages and disadvantages of the different numerical models. Numerical details on discretization effects (e.g. mesh density and orientation) and domain size were investigated in detail for practical applications. It became evident that meticulous attention to mesh resolution and domain size is imperative for achieving accurate numerical simulations, even for static cracks. Moreover, when comparing numerical methods to closed-form solutions for static cracks, all models successfully reproduced the maximum crack opening but encountered challenges near the crack tips. Finally, the paper discusses how to convert between and therefore compare parameters of various numerical approaches. Our benchmark studies reveal that each model necessitates a distinct number of parameters, even in simple scenarios like static crack aperture benchmarks. It is generally more practical to employ fewer parameters to mitigate model over-parameterization and enhance experimental feasibility.

[1] www.decovalex.org

*Corresponding authors
Keita.yoshioka@ufz.de (K. Yoshioka)
ORCID(s):

Acronyms

BPM–DEM Bonded Particle Model–Distinct Element Method

CAS Chinese Academy of Sciences

CMEFM–FEM Contact Modeling with Embedded Fracture Model–Finite Element Method

CNSC Canadian Nuclear Safety Commission

ETEL–FEM Embedded Thin Elastic Layer–Finite Element Method

GBM–DEM Grain Based Model–Distinct Element Method

hCA–FEM/xFEM Hybrid Cellular Automata–Finite Element Method/Extended Finite Element Method

IFDM–DEM Integral Finite Difference Method–Distinct Element Method

KAERI Korea Atomic Energy Research Institute

KIGAM Korea Institute of Geoscience and Mineral Resources

LIE–FEM Lower Dimensional Interface Elements–Finite Element Method

RWM/Q/UoE Radioactive Waste Management/Quintessa/University of Edinburgh

SSM/DynaFrax DynaFrax/Swedish Radiation Safety Authority

TUBAF Technische Universität Bergakademie Freiberg

UFZ Helmholtz–Centre for Environmental Research

VPF–FEM Variational Phase Field–Finite Element Method

Nomenclature

α	Biot's coefficient	–
$\bar{v}$	Standard scalar test function	
$\boldsymbol{\sigma}'$	Effective Cauchy stress tensor	Pa
$\boldsymbol{\sigma}$	Cauchy stress tensor	Pa
$\boldsymbol{\tau}$	Traction force vector	Pa
$\boldsymbol{\tau}_\Gamma$	Tangent vector to Γ	–
$\boldsymbol{\varepsilon}$	Total strain tensor	–
$\boldsymbol{\varepsilon}_\mathrm{e}$	Elastic strain tensor	–
$\boldsymbol{g}$	Gravity acceleration vector	$\mathrm{m\,s^{-2}}$
ℓ	Regularization length parameter	m
I	Second-order identity tensor	
$\mathbf{F}^n$	Contact normal force vector	N
$\mathbf{F}^s$	Contact shear force vector	N
$\mathbf{k}$	Intrinsic permeability tensor	m^2

$\mathbf{n}_\Gamma$	Normal vector to Γ	–
$\mathbf{u}$	Solid displacement vector	m
$\mathbf{u}^n$	Contact normal displacement vector	m
$\mathbf{u}^s$	Contact shear displacement vector	m
$\mathbf{u}_0$	Prescribed boundary displacement	m
$\mathbf{n}$	Normal vector	–
$\mathbf{q}_p$	Darcy velocity	$\mathrm{m\,s^{-1}}$
$\mathbf{t}_\Gamma$	Total traction	N
$\mathbf{v}$	Enriched Bubnov-Galerkin test function	
μ	Fluid dynamic viscosity	Pa s
μ_f	Friction coefficient	–
ϕ	Porosity	$\mathrm{m^3\,m^{-3}}$
ψ	Dilation angle	°
ρ	Density of the porous medium	$\mathrm{kg\,m^{-3}}$
ρ_f	Fluid density	$\mathrm{kg\,m^{-3}}$
ρ_s	Solid density	$\mathrm{kg\,m^{-3}}$
$\tilde{q}_\mathrm{F}$	Fluid exchange	
A_c	Area of the sub-contact	$\mathrm{m^2}$
c	Cohesion	Pa
G_c	Fracture toughness	Pa m
K^f	Inverse compressibility (moduli) of the fluid	Pa
K^s	Inverse compressibility (moduli) of the solid	Pa
k_n	Contact normal stiffness	$\mathrm{Pa\,m^{-1}}$
k_s	Contact shear stiffness	$\mathrm{Pa\,m^{-1}}$
p_f	Fluid pressure in the fracture	Pa
P_n	Penalty factor	$\mathrm{N\,m^{-3}}$
p_p	Fluid pressure in porous medium	Pa
q_l	Rate of leak-off between the fracture and the porous medium	$\mathrm{m^3\,s^{-1}\,m^{-2}}$
q_n	Prescribed normal flux	$\mathrm{m^3\,s^{-1}\,m^{-2}}$
q_p	Fluid velocity in the porous medium	$\mathrm{m\,s^{-1}}$
q_{ps}	Source/Sink term in the porous medium	$\mathrm{m^3\,s^{-1}\,m^{-2}}$
T_0	Contact stress at zero gap	Pa

T_n	Contact stress	Pa
v	Scalar phase-field variable	–
$W(\mathbf{u})$	Strain energy density	$\mathrm{J\,m^{-3}}$
w	Aperture	m
$\boldsymbol{C}_e$	Fourth-order elastic tensor	

1. Introduction

This work is part of the DECOVALEX project in its 8th phase, where the acronym stands for DEvelopment of COupled models and their VALidation against Experiments. DECOVALEX is an international research and model comparison project which has initiated in 1992 [1]. The focus is a better model–driven understanding of coupled thermo–hydro–mechanical–chemical processes in geosystems.

Fracture mechanics of brittle rocks related to thermo–hydro–mechanical (THM) processes is the main purpose of Task G in DECOVALEX–2023. A graphical structure of Task G with its four steps is illustrated in Figure 1.

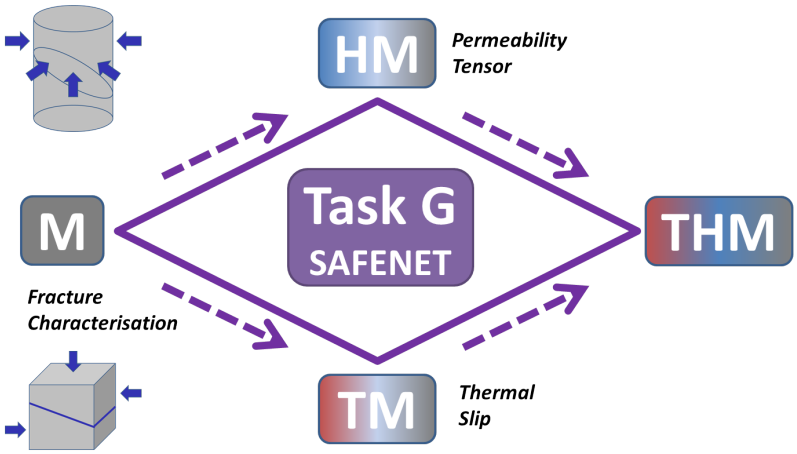

Figure 1: Overview of the Task G concept

- Step 1: Mechanical (M) results derived from constant normal load direct shear tests and constant normal stiffness direct shear tests as well as high-resolution fracture surface scans (Technische Universität Bergakademie Freiberg (TUBAF)) will build a starting point for fracture characterization.
- Step 2: Investigate hydro–mechanical (HM) results obtained with the GREAT cell (University of Edinburgh) with focus on fundamental shear processes under complex 3D stress states.
- Step 3: Investigate and model thermo–mechanical (TM) results obtained from tri–axial tests conducted at the Korea Institute of Civil Engineering and Building Technology (KICT) with focus on shear processes triggered by thermal stresses.
- Step 4: Combining and upscaling near–field approaches for THM analysis.

The general concept of Task G is organized into a verification component followed by a validation phase. The verification procedure is conducted first by systematic benchmark exercises (this paper) and then by analysis of given experimental data. The validation procedure is based on blind predictions of experimental data (not known a–priori) to test the physical validity of the model. The final goal of Task G is upscaling fracture mechanics processes from the

laboratory to the field scale. A common tool of DECOVALEX for the verification–validation procedure is model and code comparison by the participating teams.

This paper focuses on the systematic benchmark tests for hydro–mechanical (HM) coupled fracture mechanics and examines a large variety of methods for this purpose such as Variational Phase Field–Finite Element Method (VPF–FEM) by Helmholtz–Centre for Environmental Research (UFZ), Hybrid Cellular Automata–Finite Element Method/Extended Finite Element Method (hCA–FEM/xFEM) by Chinese Academy of Sciences (CAS), Lower Dimensional Interface Elements–Finite Element Method (LIE–FEM) by TUBAF, Contact Modeling with Embedded Fracture Model–Finite Element Method (CMEFM–FEM) by Radioactive Waste Management/Quintessa/University of Edinburgh (RWM/Q/UoE), Embedded Thin Elastic Layer–Finite Element Method (ETEL–FEM) by Canadian Nuclear Safety Commission (CNSC), Grain Based Model–Distinct Element Method (GBM–DEM) by Korea Institute of Geoscience and Mineral Resources (KIGAM), Bonded Particle Model–Distinct Element Method (BPM–DEM) by DynaFrax/Swedish Radiation Safety Authority (SSM/DynaFrax) and Integral Finite Difference Method–Distinct Element Method (IFDM–DEM) by Korea Atomic Energy Research Institute (KAERI) in Section 2. Two basic types of benchmarks have been used, static and propagating fractures with different geometries (Section 3). Benchmark results are compared against classical analytical solutions. The following aspects have been addressed: differences in numerical treatment/approximation/assumption of fracture, differences in extra parameters introduced/required in addition to the fracture mechanics theory, and equivalences/conversions of the parameters amongst the models (Section 4). The lessons learned from the benchmarks studies and next steps in Task G are summarized in Section 5.

2. Methods

This study focuses on the hydro-mechanical responses of a fractured rock under various controlled stress magnitudes and orientations. In Section 2.1, we summarize the governing equations for poroelastic deformation, fluid flow in porous media, and fluid flow in fractures. Furthermore, we briefly introduce the various numerical methods that were involved in this project in Section 2.2.1.

2.1. Governing equations

Poro–elastic deformation description. The theory of linear poroelasticity proposed by Biot has generally been used to model reservoir deformation [2]. By introducing the poroelastic effective stress $\boldsymbol{\sigma}' := \boldsymbol{\sigma}(\mathbf{u}) + \alpha p_p \mathrm{I}$, and under the assumptions of quasi–statics, the governing equations for the poroelastic deformation read:

$$\nabla \cdot \left(\boldsymbol{\sigma}' - \alpha p_p \mathrm{I}\right) + \rho \boldsymbol{g} = \mathbf{0} \qquad \text{in } \Omega \setminus \Gamma, \tag{1}$$

$$\boldsymbol{\sigma} \cdot \mathbf{n} = \boldsymbol{\tau} \qquad \text{on } \partial\Omega_N^m, \tag{2}$$

$$\mathbf{u} = \mathbf{u}_0 \qquad \text{on } \partial\Omega_D^m, \tag{3}$$

$$\boldsymbol{\sigma}^{\pm} \cdot \mathbf{n}_{\Gamma^{\pm}} = -p_f \mathbf{n}_{\Gamma^{\pm}} \qquad \text{on } \Gamma^{\pm}, \tag{4}$$

where the density of porous medium is composed of both fluid and solid densities, $\rho = \phi\rho^f + (1-\phi)\rho^s$. The constitutive relation for a poro–elastic material can be written as

$$\mathrm{d}\boldsymbol{\sigma}' = \boldsymbol{C}_{\mathrm{e}} : \mathrm{d}\boldsymbol{\varepsilon}_{\mathrm{e}},$$

where $\boldsymbol{\varepsilon}_{\mathrm{e}} = \frac{1}{2}(\nabla\mathbf{u} + (\nabla\mathbf{u})^T) = \nabla^s\mathbf{u}$ is the linearized strain.

Porous medium fluid flow description. The mass conservation with the momentum balance stated in the form of Darcy's law leads to the governing equations of fluid flow in a porous medium:

$$\rho\left(\frac{\alpha-\phi}{K^s} + \frac{\phi}{K^f}\right)\frac{\partial p_p}{\partial t} + \rho\alpha\nabla\cdot\frac{\partial\mathbf{u}}{\partial t} + \nabla\cdot(\rho\mathbf{q}_p) = \rho q_{ps} \qquad \text{in } \Omega \setminus \Gamma, \tag{5}$$

$$\rho\mathbf{q}_p = -\frac{\rho\mathbf{k}}{\mu}(\nabla p_p - \rho^f\mathbf{g}) \qquad \text{in } \Omega \setminus \Gamma, \tag{6}$$

$$p_p = \bar{p}_p \qquad \text{on } \partial_D^f\Omega, \tag{7}$$

$$\rho\mathbf{q}_p \cdot \mathbf{n} = \rho q_n \qquad \text{on } \partial_N^f\Omega, \tag{8}$$

Table 1
Numerical methods and codes

Team	Numerical methods	Codes
UFZ	VPF–FEM	OpenGeoSys-6 (Section 2.2.1)
CAS	hCA–FEM/xFEM	CASRock (Section 2.2.2)
TUBAF	LIE–FEM	OpenGeoSys-6 (Section 2.2.3)
CNSC	ETEL–FEM	COMSOL (Section 2.2.5)
RWM/Q/UoE	CMEFM–FEM	COMSOL (Section 2.2.4)
KIGAM	GBM–DEM	3DEC (Section 2.2.6)
SSM/DynaFrax	BPM–DEM	PFC (Section 2.2.7)
KAERI	IFDM–DEM	TOUGH/3DEC (Section 2.2.8)

Fracture Fluid flow description. Reynolds' lubrication model is generally used to simulate fluid flow in fractures under the assumption of a low Reynolds number and constant pressure in the orthogonal direction to the flow. The governing equations of the fluid inside the fracture read:

$$\frac{\partial(\rho w)}{\partial t} - \nabla_\Gamma \cdot \left(\rho \, \frac{w^3}{12\mu} \nabla_\Gamma p_f \right) + \rho q_l = \rho q_{fs} \qquad \text{in } \Gamma, \tag{9}$$

$$\rho q_l = -[\![\rho \mathbf{q}_p]\!] \cdot \mathbf{n}_\Gamma \qquad \text{on } \Gamma, \tag{10}$$

$$-\rho \, \frac{w^2}{12\mu} (\nabla_\Gamma p_f - \rho^f \mathbf{g}) \cdot \boldsymbol{\tau}_\Gamma = 0 \qquad \text{on } \partial\Gamma. \tag{11}$$

2.2. Numerical methods

There exists several works on the numerical modeling of hydro–mechanical responses in fractured rock. Generally, they can be classified into two types of approaches, *sharp fracture approaches* (xFEM and *etc.*) and *diffuse fracture approaches* (phase-field models). In this study, eight teams collaborate to simulate and predict the hydro–mechanical reaction of fractured rock using different numerical method and computing packages, Table 1.

2.2.1. VPF–FEM

Numerical method. Variational phase-field for fracture models have become one of the most extensively used methods to simulate fracture propagation for a number of applications such as brittle [3, 4, 5], ductile [6, 7, 8, 9], dynamic [10, 11, 12, 13] , fatigue [14, 15], interface [16, 17], desiccation [18, 19], environment assisted [20, 21, 22], and hydraulic fracturing [23, 24, 25, 26, 27, 28]. Their popularity stems from their ability to represent the complex evolution of any number of fractures without confining their propagation to any specific grid.

Mathematical model. Griffith's criterion was reformulated by Francfort and Marigo [29] as the minimization of total energy, which is the sum of potential and fracture surface energy defined as:

$$\mathcal{F}(u, \Gamma) := \int_{\Omega \setminus \Gamma} W(\mathbf{u}) \, \mathrm{d}\Omega + \int_\Gamma G_\mathrm{c} \, \mathrm{d}\Gamma, \tag{12}$$

the strain energy density and fracture toughness are represented by $W(\mathbf{u})$ and G_c, respectively. Evaluating the crack surface energy for non-trivial crack geometry is challenging since it includes the surface integral over an evolving discrete crack set Γ. To address this issue, the variational phase-field approach presented in [3] follows the approximation of [30] via Γ-convergence [31]. The energy functional is regularized [3] by introducing a scalar phase-field variable, $v : \Omega \mapsto [0, 1]$ and a regularization length parameter $\ell > 0$,

$$\mathcal{F}_\ell := \int_\Omega v^2 W(\mathbf{u}) \, \mathrm{d}\Omega + \int_\Omega \frac{G_c}{4c_n} \left(\frac{(1-v)^n}{\ell} + \ell |\nabla v|^2 \right) \mathrm{d}\Omega. \tag{13}$$

The work done by fluid pressure, $\int_\Gamma p_f \, [\![\mathbf{u} \cdot \mathbf{n}]\!] \, \mathrm{d}\Gamma$, can be added to the total energy function, where p_f is the "net" pressure defined as the surplus pressure above the minimum stress and $\mathbf{n}$ is the normal vector to Γ. The amount of jump

over Γ might be approximated as [23, 32]:

$$\int_\Gamma p_f \, [\![\mathbf{u}\cdot\mathbf{n}]\!] \, \mathrm{d}\Gamma \approx \int_\Omega p_f \, \mathbf{u}\cdot\nabla v \, \mathrm{d}\Omega.$$

Because the toughness-dominated hydraulic fracturing regime takes no pressure loss in the crack into account, our total energy is as follows:

$$\mathcal{E}_\ell := \int_\Omega v^2 W(\mathbf{u}) \, \mathrm{d}\Omega + \int_\Omega \frac{G_c}{4c_n}\left(\frac{(1-v)^n}{\ell} + \ell|\nabla v|^2\right) \mathrm{d}\Omega + p_f \int_\Omega \mathbf{u}\cdot\nabla v \, \mathrm{d}\Omega. \tag{14}$$

Therefore we minimize (14) with the mass balance constrain as follows:

$$(\mathbf{u}_i, v_i; p_f) = \operatorname{argmin}\left\{\mathcal{E}_\ell(\mathbf{u}, v; p) \,:\, \mathbf{u}\in\mathcal{U}(t_i), v\in\mathcal{V}(t_i, v_{i-1}), Q_i = \int_\Omega \mathbf{u}\cdot\nabla v \, \mathrm{d}\Omega\right\}. \tag{15}$$

Computing package. The current model is implemented in an open-source code, OpenGeoSys [33]. OpenGeoSys (OGS) is an open-source scientific project that aims to develop numerical methods for simulating thermo-hydro-mechanical-chemical (THMC) processes in porous and fractured media. More information concerning the code and simulation examples are freely available at `https://www.opengeosys.org/`.

2.2.2. hCA–FEM/xFEM

Numerical method. Cellular automata uses a local updating rule to solve the state variables. According to cellular automata localization theory, only the states of the cell itself and its neighbours contribute to the state of the cell. We can develop the updating rule for displacement, temperature and fluid pressure using local equilibrium conditions, in which the local stiffness is taken from the element stiffness of FEM/xFEM [34, 35]. The hybrid cellular automata scheme avoids the solution of large linear equations and the complexity herein. To represent the fracture, interface elements or Goodman elements, internal interfaces or internal boundaries, and weak elements, are implemented .

In this study, the fluid flow and mechanical processes are sequentially coupled. The fluid mass balance and momentum balance equations are expressed in Section 2.1. The equations can be solved via spatial and temporal discretization. Instead of using traditional numerical methods, cellular automata technique is used for the solution of displacement and fluid pressure on spatial scale by developing the local updating rule according to the local equilibrium conditions,

$$\mathbf{K}_{ij}\Delta\boldsymbol{H}_j = \Delta Q_i, \tag{16}$$

where $\mathbf{K}_{ij}$ is the local nodal stiffness matrix, which is summation of stiffness of cell elements related to the cell node. $\Delta\boldsymbol{H}_j$ is the incremental value of physical variable; ΔQ_i is the incremental value of source term. When the incremental value of physical variable is obtained, the incremental value of source term at its neighbour cell nodes can be solved. The neighbour cell nodes will follow the same rule and the global calculation is divided into the iterations of cells one by one. On temporal scale, an explicit finite difference scheme is used. The equation of the time derivative of specified physical variable as a column vector is listed below,

$$\{\frac{\partial\boldsymbol{H}}{\partial t}\}_t = \frac{1}{\Delta t}(\boldsymbol{H}_t - \boldsymbol{H}_{t-\Delta t}) + o(\Delta t), \tag{17}$$

where $o(\Delta t)$ is an error item and

$$\{\frac{\partial\boldsymbol{H}}{\partial t}\} = \{(\frac{\partial\boldsymbol{H}_1}{\partial t}) \quad (\frac{\partial\boldsymbol{H}_2}{\partial t})\cdots(\frac{\partial\boldsymbol{H}_n}{\partial t})\}^T, \tag{18}$$

weak elements approach are chosen for fracture representation [36]. For a weak element, the stiffness of the element depends on the size of the element and a simple formula is used for selecting the appropriate Young's modulus for the element, i.e.,

$$\frac{1}{E_f} = \frac{1}{E_r} + \frac{1}{(k_n\times b)}, \tag{19}$$

where E_f and E_r are Young's modulus of fracture and rock matrix element, respectively. k_n is the normal stiffness of fracture and b is the mean size of fracture element, which can be defined as the square root of fracture element area.

Computing package. The model is based on a self–developed software, CASRock, which is based on cellular automata, FEM and xFEM [37, 38, 39, 40]. CASRock is a versatile software that can be used to simulate rock failure processes, tunnel excavation, multi-field coupling, dynamic load effects, and more. Further information about the software can be found at `www.casrock.cn`.

2.2.3. LIE–FEM

Numerical method. A diverse range of methods exists to capture fractures in porous media as embedded lower-dimensional continua [41, 42, 43, 44, 45, 46, 47]. This lower–dimensional representation is often achieved by integrating over one spatial dimension—usually the fracture thickness—subject to a set of assumptions, such as parallel–plate flow. The lower-dimensional interface element (LIE) method has been developed to enhance the capability of simulating hydraulic fracturing and shearing [48, 49]. Several constitutive formulations for the hydraulic and mechanical behaviour of the discrete interface are available, such as elasto-plasticity or cohesive-zone models.

Mathematical model. A coupled hydraulic-mechanical problem is solved on a domain $\Omega = \Omega^+ \cup \Omega^-$ separated into the two indicated parts by a sharp interface Γ representing the fracture. The weak form of the mechanical problem reads

$$\int_{\Omega\setminus\Gamma} \left[\boldsymbol{\sigma} : \nabla\mathbf{v} - \varrho\mathbf{g}\cdot\mathbf{v}\right] \mathrm{d}\Omega - \int_{\Gamma} \boldsymbol{\tau}_\Gamma \cdot [\![\mathbf{v}]\!]_\Gamma \,\mathrm{d}\Gamma = \int_{\partial\Omega} \boldsymbol{\tau}\cdot\mathbf{v}\,\mathrm{d}\Gamma, \tag{20}$$

where an enriched Bubnov-Galerkin test function $\mathbf{v}$ of the same space as the solid displacement itself was introduced, consisting of a continuous (standard) part $\mathbf{v}_\mathrm{c}$ and a Heaviside enrichment $H(\mathbf{x})\mathbf{a}_\Gamma$ in the form

$$\mathbf{v} = \mathbf{v}_\mathrm{c} + H(\mathbf{x})\mathbf{a}_\Gamma, \tag{21}$$

with the Heaviside function $H(\mathbf{x}) = \pm 0.5\ \forall \mathbf{x} \in \Omega^\pm$ distinguishing the domains separated by the fracture.

Note that $\boldsymbol{\sigma}$ and $\mathbf{t}_\Gamma$ are the total stresses and tractions, respectively, in a HM formulation of a fluid-saturated porous medium in the sense of the effective stress principle:

$$\boldsymbol{\sigma} = \boldsymbol{\sigma}' - \alpha p_p \mathbf{I} \quad \text{with} \quad \mathrm{d}\boldsymbol{\sigma}' = \boldsymbol{C}_\mathrm{e} : \mathrm{d}\boldsymbol{\varepsilon}_\mathrm{e} \tag{22}$$

$$\boldsymbol{\tau}_\Gamma = \boldsymbol{\tau}'_\Gamma - p_p \mathbf{n}_\Gamma \quad \text{with} \quad \mathrm{d}\boldsymbol{\tau}'_\Gamma = \mathbf{K}^\mathrm{f}\mathrm{d}\mathbf{w}^\mathrm{e}. \tag{23}$$

The weak form for matrix flow based on a standard scalar test function $\bar{v}$ reads

$$\int_{\Omega} \bar{v}\left[S p'_\mathrm{S} + \alpha\nabla\cdot\mathbf{u}'_\mathrm{S} - \delta_\Gamma(\mathbf{x})\tilde{q}_\mathrm{F}\right] - \mathbf{q}_p\cdot\nabla\bar{v}\,\mathrm{d}\Omega = \int_{\partial\Omega}\bar{v}q_\mathrm{n}\,\mathrm{d}\Gamma, \tag{24}$$

with the Darcy velocity $\mathbf{q}_p$. The fluid exchange $\tilde{q}_\mathrm{F}$ is active only at fractures where the following weak form is used:

$$\int_{\Gamma} \bar{v}_\Gamma\left[b'_\mathrm{S} + bS^\mathrm{f}p'_\mathrm{S} + b\tilde{q}_\mathrm{F}\right] - b\mathbf{q}_p^\Gamma\cdot\nabla_\Gamma\bar{v}_\Gamma\,\mathrm{d}\Gamma = \int_{\partial\Gamma}\bar{v}_\Gamma q_\mathrm{n}^\Gamma\mathrm{d}l. \tag{25}$$

The mass exchange between fractures and matrix remains implicit as the current implementation assumes local mass exchange processes between matrix and fracture to be sufficiently fast to ensure pressure continuity between both compartments.

Computing package. The present model is implemented in the scientific open-source finite element software OpenGeoSys [33, 50].

2.2.4. CMEFM–FEM

Numerical method. The RWM/Quintessa/UoE team applied a full contact representation of the embedded fracture using the COMSOL Multiphysics® Structural Mechanics module [51], with an internal boundary load applied to either side of the fracture to represent the fluid pressure. This approach allows the possibility of representing opening, friction, separation, and other complex non-linear behaviours at the fracture surface, though only the zero friction case is considered in the benchmark. The remainder of the domain is modelled as an elastic rock medium.

Mathematical model. The main equation for solving the system is standard solid mechanics solving for displacement. Full details of this approach are in the COMSOL Multiphysics® Structural Mechanics module User Guide [51].

The contact boundary pair(s) representing the fracture is used to introduce contact forces when in contact; when there is a gap, there is no contact and thus no contact force. By its nature, this method can be highly non-linear and therefore can be difficult to solve. For this benchmark model, a penalty factor formulation is used which describes a spring stiffness of two connecting boundaries in contact, defining the contact stress, which allows some (potentially nonphysical) penetration as the contacts are forced together. The contact stress is governed by:

$$T_n = \begin{cases} -P_n g_n + T_0 & \text{if } g_n \leq \frac{T_0}{p_n} \\ 0 & \text{otherwise.} \end{cases} \tag{26}$$

Here, T_n and T_0 are the contact stress and contact stress at zero gap; g_n is the gap; and P_n is the penalty factor that is tuned to give the required contact elasticity.

Computing package. COMSOL Multiphysics® using the Structural Mechanics module. COMSOL Multiphysics® is a commercial application for simulation and coupled process modelling using the finite element method.

2.2.5. ETEL–FEM

Numerical method. The finite element method, implemented in the commercial software COMSOL Multiphysics® [51], was used to numerically solve the governing equations of the mathematical model. Solid serendipity elements are used to represent the intact granite, with cubic shape functions for the mechanical behaviour, and linear shape functions for the flow behaviour. The fracture is represented as an interface with springs shear and normal directions that connect adjacent solid elements. The normal and shear stresses across the fracture are proportional to the relative shear and normal displacements through the spring constants.

Mathematical model. The mathematical model was developed from the theory of poro–mechanics [52], with the governing equations in Section 2.1.

Computing package. The model was implemented in the COMSOL Multiphysics package. COMSOL solves partial differential equations using the finite element method. The Structural Mechanics and Darcy's flow modules of COMSOL were used in this work. For more information: `www.comsol.com`.

2.2.6. GBM–DEM

Numerical method. In a grain-based model (GBM), the microstructure of rock–like material is represented as a group of angular particles. Particles can be rigid or deformable (elastic or inelastic), while interfaces are treated as boundary conditions between particles. The interaction of the particles (blocks) and their interfaces (contacts) is calculated using a distinct element method (DEM) [53, 54, 55, 56].

Mathematical model. The calculation in the DEM alternates between the application of a force-displacement law at all contacts and Newton's second law for all blocks. At each timestep, the integration of the law of motion provides the new block positions resulting from the known forces acting on the blocks. The contact forces are then updated from the force-displacement law and known displacements. The elastic force increments at contact are calculated as

$$\Delta \boldsymbol{F}^n = -k_n \Delta \mathbf{u}^n A_c \tag{27}$$

$$\Delta \boldsymbol{F}^s = -k_s \Delta \mathbf{u}^s A_c. \tag{28}$$

where $\boldsymbol{F}^n$ is the contact normal force, $\boldsymbol{F}^s$ are the contact shear force vectors, k_n is the contact normal stiffness, k_s is the contact shear stiffness, $\mathbf{u}^n$ is the contact normal displacement, $\mathbf{u}^s$ are the contact shear displacement vectors, and A_c is the area of the sub-contact.

The contact model approximates linear representation of stiffness and yield limit, considering the displacement-weakening as a result of loss in frictional, cohesive, and tensile strength at the onset of failure. If the maximum limit for normal force or shear force is exceeded, the onset of failure is identified at the sub-contact, and the new contact forces are corrected.

The hydro–mechanical simulation is performed by sequentially alternating mechanical calculation and fluid calculation. The fluid flow inside the fracture (zero-strength contacts or failed contacts) is approximated by two-dimensional horizontal flow within parallel walls separated by a hydraulic aperture. The hydraulic aperture is updated by the elastic opening, $\mathbf{u}_e^n$, due to the change in effective normal stress and the plastic opening, $\mathbf{u}_p^n$, due to slip-induced dilation:

$$\Delta \mathbf{u}_p^n = \Delta \boldsymbol{\sigma}_n' / k_n \tag{29}$$

$$\Delta \mathbf{u}_p^n = \mathbf{u}_p^s \tan \psi, \tag{30}$$

where $\boldsymbol{\sigma}_n'$ is the effective normal stress, $\mathbf{u}_p^s$ is the plastic shear displacement, and ψ is the dilation angle.

The flow rate per unit width of the fractures is characterized by the cubic law [57]. The fracture pressures are calculated and stored in the flow elements corresponding to the grid points of blocks. After flow rate calculations, the pressures are updated taking into account the net flow into the flow element and possible changes in flow element volume due to the incremental motion of the surrounding blocks:

$$\Delta p_f = K^f Q \frac{\Delta t}{V} - K^f \frac{\Delta V}{V_m}, \tag{31}$$

where K^f is the bulk modulus of the fluid, Q is the sum of flow rates into the flow element from all surrounding contacts, Δt is the timestep, V is the flow element volume, and V_m is the average flow element volume of the previous and current timesteps.

Computing package. The above approach is implemented into the commercial code 3DEC [58], a three–dimensional DEM code. In the benchmark exercises, we generated a dense assemblage of tetrahedral blocks. The blocks were assumed to behave elastically, and the embedded single fracture was assigned the Coulomb slip model.

2.2.7. BPM–DEM

Numerical method. In a bonded particle model (BPM), a material is simulated as an aggregate of rigid particles (2D: disks, 3D: spheres) bonded at their contact points with finite stiffness and strength [59]. The numerical method is called hydro–mechanical–coupled BPM, and hydro–mechanical coupled concept is developed and implemented in a BPM [60].

Mathematical model. A flow of viscous fluid in a BPM and fluid pressures and volume driven breakages of bonds are simulated. The concept of fluid flow algorithm is proposed by Cundall (unpublished technical note, 2000), which was later modified by Hazzard *et al.* [60] and further modification was done by Yoon *et al.* [61, 62]. The pressure–driven flow of viscous fluid between the two pore spaces is governed by the cubic law assuming that the flow is laminar between two smooth parallel plates

A hydraulic aperture w of the flow channel changes as a function of stress, σ_n. In this HM benchmark modelling, we use experimentally derived w vs. σ_n relation from Hökmark *et al.* [63]:

$$w = w_{inf} + \left(w_0 - w_{inf}\right) \exp(-0.15\sigma_n) \tag{32}$$

where, w_{inf} is the hydraulic aperture at an infinite normal stress, w_0 is the hydraulic aperture at no normal stress. We compute the fluid pressure increase per time step Δt in a pore space using,

$$\Delta p_f = \frac{K^f}{V_d}(Q \Delta t), \tag{33}$$

where, K^f is the fluid bulk modulus, V_d is the pore volume, Q is the sum of net flow rates in a pore volume. The fluid pressure exerts traction on the surrounding particles. As a result, the particles displace, and the stress state at particle contact changes which in turn changes the hydraulic aperture and thereby the flow field. This is two–way full coupling between the particles (solid part) and the pore fluid (fluid part).

Computing package. The modelling concept and mathematical formulation are implemented in the commercial code Particle Flow Code 2D (PFC2D), a two–dimensional distinct element geomechanical modelling software [64], using FISH programming.

2.2.8. IFDM–DEM

Numerical method. The integral finite difference method (IFDM) for thermal–hydraulic analysis [65] is coupled with the distinct element method for discontinuum mechanical analysis [66], to describe the thermal–hydraulic–mechanical analysis of fractured rock mass [67]. The discontinuum model consists of tetrahedral meshes and discontinuity faces, and the discontinuities are assumed as elements with aperture–size width for the thermal–hydraulic analysis in IFDM. IFDM and DEM exchange and reflect the thermal, hydraulic, and mechanical parameters in each time step of IFDM.

Mathematical model. The mechanical analysis is based on the interactions between blocks due to the movements and rotations in DEM module. The interactions are calculated by Newton's second law on each face of blocks and the force–displacement law on each contact between blocks (Equations (27) and (28)). The contacts between blocks represent the discontinuities, and the detailed mechanical models can be applied on each contact. In this study, the linear normal and shear deformation models are assumed with the shear and tensile failure. When the normal and shear stresses reach the tensile and shear strength of the discontinuity, the normal and shear stress yield and induce the plastic displacement. Both elastic and plastic displacements in the normal direction on discontinuities accompany the hydraulic aperture change, and the shear displacement also can induce the dilation of aperture based on the dilation angle, which is the parameter regarding the discontinuity roughness. The permeabilities of discontinuities are updated based on the hydraulic aperture change and the cubic law [57]. The updated permeability field in every mechanical simulation is transferred to IFDM module for hydraulic analysis.

IFDM module constructs the elements and connections data for hydraulic analysis. The discontinuity elements have appropriate hydraulic properties equivalently calculated or updated from the mechanical analysis. The fluid flow in IFDM module is based on the mass balance equation between two adjacent elements. The mass balance equation includes the multiphase and multicomponent fluid flow [65].

$$\frac{d}{dt}\int_{\Omega} M^i \, d\Omega = \int_{\partial\Omega} \mathbf{j}^i \cdot \mathbf{n} \, d\Gamma + \int_{\Omega} q^i \, d\Omega, \tag{34}$$

where, Ω is the volume of an arbitrary domain, $\partial\Omega$ is the closed surface of the domain with the normal vector $\mathbf{n}$, M is the mass per volume, $\mathbf{j}$ is the mass flux, q is the mass source/sink, and i denotes each component. The mass flux consists of individual phase fluxes calculated by Darcy's law.

$$\mathbf{j}^{\beta} = \rho^{\beta}\mathbf{q}_p^{\beta}, \tag{35}$$

where, $\mathbf{j}^{\beta}$ is the mass flux of phase β, ρ^{β} is the density of phase β, $\mathbf{q}_p^{\beta}$ is the Darcy velocity in phase β. According to the mass balance equation, the pore pressures on whole elements are updated, and the pore pressure data is transferred to DEM module to be reflected for the mechanical analysis in every hydraulic time step.

Computing package. The model in this study is implemented in TOUGH2, a numerical simulator for multi dimensional, multiphase, multicomponent fluid flows and heat transfer [65], and 3DEC, a block–based three–dimensional distinct element method [66]. Additional TOUGH–3DEC linking algorithms for the coupled processes are developed in FISH, FORTRAN, and MATLAB [67].

3. Benchmark Exercises

This section contains a set of benchmarks to verify the hydro–mechanical process in various simulation packages. First, we compared the fracture aperture with Sneddon's solution (static) [68]. Second, we verified the model with plane-strain hydraulic fracture propagation in a toughness dominated regime based on Sneddon's solution [68]. To account for the infinite boundaries in Sneddon's closed-form solution, we considered a large finite domain. Third, we conducted a benchmark with the same domain size as the laboratory experiment while applying differential stresses at the boundaries. Fourth, the third benchmark was repeated with an inclined fracture. Lastly, we provide mesh and domain studies. Figure 2 summarizes the overviews of benchmarks. Table 2 lists the material properties.

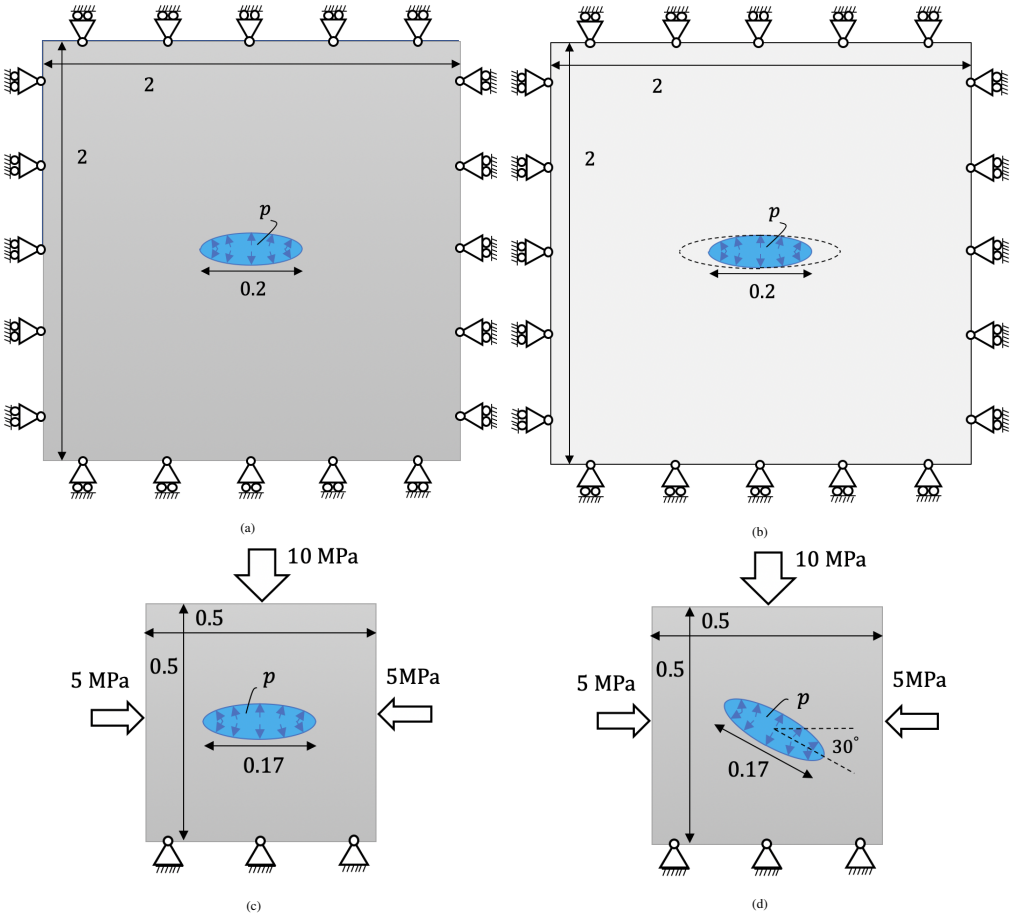

Figure 2: Benchmarks overview. (a) *benchmark 1*: static horizontal fracture under a constant pressure, (b) *benchmark 2*: propagating horizontal fracture in the toughness dominated regime, (c) *benchmark 3*: static horizontal fracture under a constant pressure with differential in–situ stress and (d) *benchmark 4*: static inclined fracture under a constant pressure with differential in–situ stress. The unit of domain sizes is meter [m].

3.1. Benchmark 1: static fracture aperture under a constant pressure

A line fracture $[-a_0, a_0] \times \{0\}$ ($a_0 = 0.1$m) with no external loading and an internal fluid pressure of $p = 1$ MPa was applied on the fracture surfaces and we compared the fracture aperture with the analytical solution [70] (p. 29) for the fracture half-opening:

$$u(x,0) = \frac{2pa_0}{E'}\sqrt{1-(x/a_0)^2}, \tag{36}$$

where u is the displacement E' is the plane strain Young's modulus ($E' = E/(1-\nu^2)$) with ν is Poisson's ratio, p is the fluid pressure inside the fracture. To account for the infinite boundaries in the closed-form solution, we considered a large finite domain $[-10a_o, 10a_o] \times [-10a_o, 10a_o]$ (Figure 2). The effective element size, h, is 1×10^{-3} m.

Computed fracture half–aperture and error profiles from different numerical methods are compared against the analytical solution (Eq. (36)) in Figure 3. The errors are computed as a difference from the closed form solution. The error profiles demonstrate that the aperture in the middle of the fracture is in good agreement with the close form solution, however near the fracture tip, most numerical solutions are highly inaccurate.

3.2. Benchmark 2: Propagating fracture in the toughness dominated regime

Under the toughness dominated regime without leak-off, the energy dissipation by the fluid viscosity is negligible compared with the energy released for the fracture surface creation [71]. Therefore, in this regime, we can neglect the

Table 2
Rock parameters of granite used in the direct shear tests [69].

Name	Symbol	Value	Unit
Young's modulus	E	49.75×10^9	Pa
Fracture toughness †	K_I	0.95×10^6	Pa · $m^{1/2}$
Poisson's ratio	ν	0.26	–
Compressive strength	σ_c	120.54×10^6	Pa
Tensile strength	σ_t	7.02×10^6	Pa
Friction angle (Mohr)	ϕ	52.5	°
Basic Friction angle (Mohr)	ϕ_b	30	°
Cohesion	c	22.5×10^6	Pa

†$G_c = K_I^2(1-\nu^2)/E$

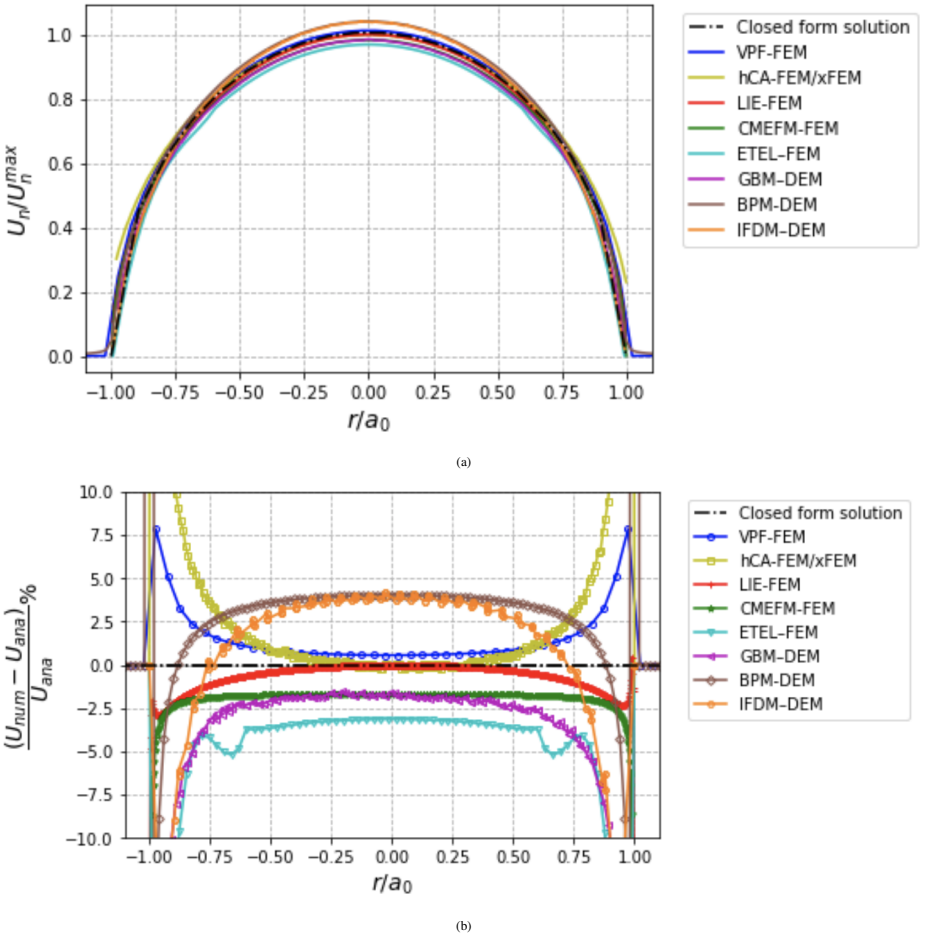

Figure 3: (a) Fracture half–aperture profiles and (b) error from different numerical methods compared against the closed-form solution.

pressure loss within the fracture and can derive the pressure and the length evolution using Eq.(36) [72, 73, 23, 74, 75, 76, 77]. From Eq.(36), we have the work of the pressure force as

$$\mathcal{W}(R) = \frac{2p^2a^2}{E'}. \tag{37}$$

Applying Clapeyron's theorem, the elastic energy is

$$\mathcal{E}(R) = -\frac{\pi p^2 a^2}{E'}, \tag{38}$$

and the energy release rate with respect to the crack length a_o propagating along the initial inclination is

$$G(R) = -\frac{\partial \mathcal{E}}{\partial(2a)} = \frac{\pi p^2 a}{E'}. \tag{39}$$

According to Griffith's criterion [78], in a quasi-static volume control setting[1], the fracture propagates when $G = G_c$ and the critical volume for crack propagation is $V_c := \sqrt{\frac{4\pi G_c a^3}{E'}}$. The corresponding pressure and the fracture length evolution are:

$$p(V) = \begin{cases} \dfrac{E'V}{2\pi a_o^2} & \text{for} V < V_c \\ \left[\dfrac{2E'G_c^2}{\pi V}\right]^{\frac{1}{3}} & \text{for} V \geq V_c, \end{cases} \tag{40}$$

$$a(V) = \begin{cases} a_o & V < V_c \\ \left[\dfrac{E'V^2}{4\pi G_c}\right]^{\frac{1}{3}} & V \geq V_c. \end{cases} \tag{41}$$

The normalized pressure p_f/p_c and the normalized crack length$/a_0$ are plotted against the normalized volume V/V_c in Figs 4. While VPF–FEM slightly overestimates the peak pressure, LIE–FEM slightly underestimates it. As the crack grows, both converge to the closed–form solution curve.

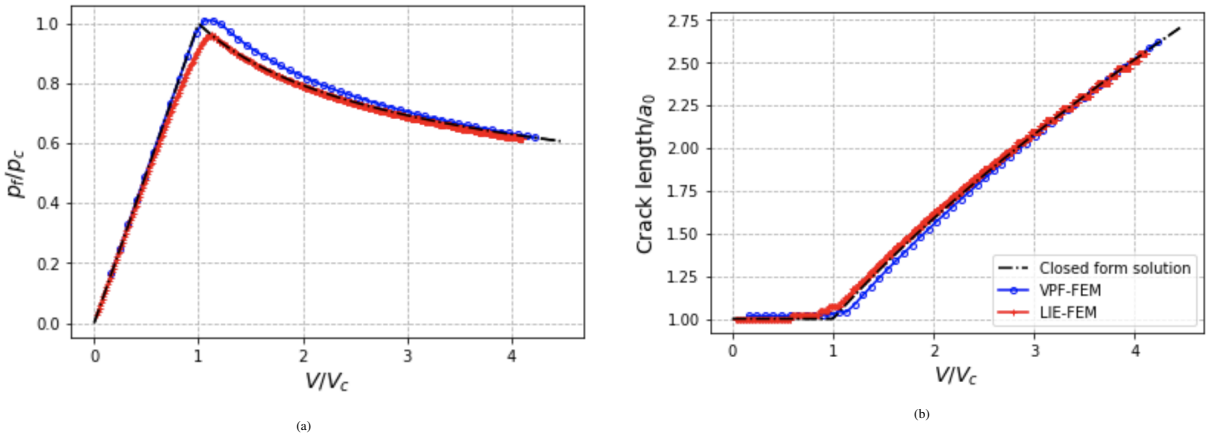

Figure 4: (a) Pressure and (b) fracture length evolution against injected volume

3.3. Benchmark 3: Static straight fracture under constant pressure with differential in–situ stress

To compare our results with laboratory experiments, we conducted a static benchmark with horizontal fracture and a sample size of 0.5 m × 0.5 m. The total length of fracture is 0.17 m. The fluid pressure within the fracture gives $p = 12$ MPa. The material properties are listed in Table 2.

Figure 5 shows the aperture profiles for the Granite specimen with a plane horizontal fracture. The aperture profiles reveal that there is a 2 μm discrepancy between different numerical approaches, which could be related to the presence of in–situ stresses and the influence of computational domain size.

[1]The fracture propagation is always unstable with pressure control.

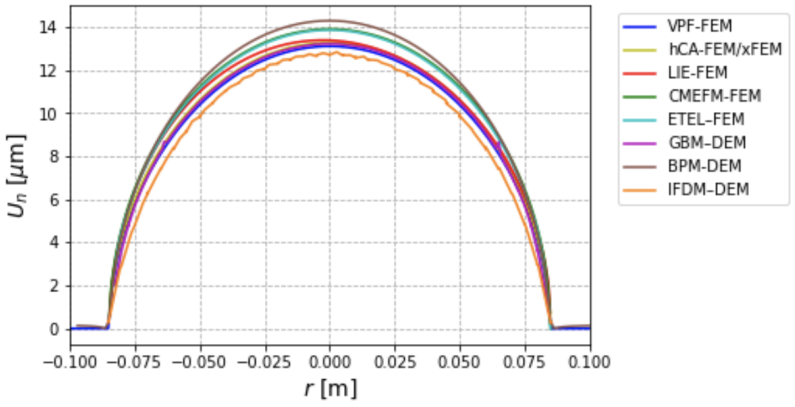

Figure 5: Aperture profile for the Granite specimen with a plane horizontal fracture.

3.4. Benchmark 4: Static inclined fracture under constant pressure with differential in–situ stress

To account for the effect of inclination, we replicated benchmark 3 with an inclined fracture. The fracture is inclined by 30° to horizontal. The remaining material and geometrical properties are identical to those of benchmark 3.

Figure 6 shows the aperture profiles for the granite specimen with an inclined fracture. In comparison to horizontal fracture in Benchmark 3, the fracture inclination dominated the discrepancies between the results of different approaches.

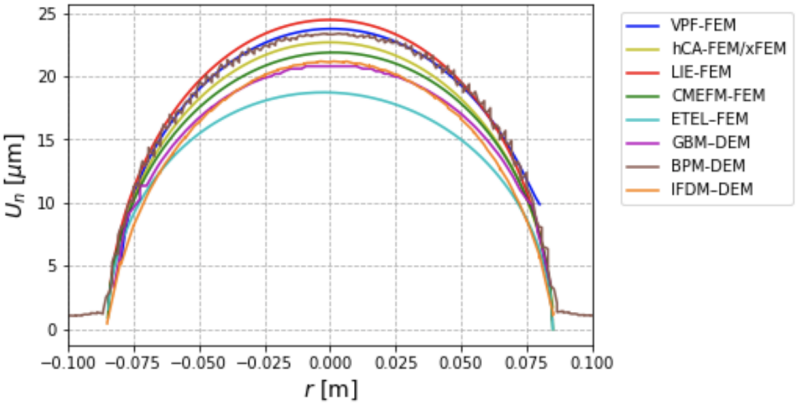

Figure 6: Aperture profiles for the Granite specimen with a plane inclined 30° fracture.

3.5. Mesh studies

This section investigates the numerical aspects of discretization effects such as mesh size and orientation.

3.5.1. Mesh size effect

We studied a mesh sensitivity by analyzing the convergence of the aperture profile for different mesh discretizations. We repeated benchmark 1 with varying mesh sizes, $h = 0.001, 0.003, 0.006$, and 0.01 m (Figure 7). As can be seen in Figure 7b, for hCA–FEM/xFEM, the results converge when $h = 0.003$m, arriving at a slightly higher profile than the closed–form solution. That is possibly explained by the fact that a softer elastic material representing the fracture may be dependent on the choices of the material properties. Figure 7c shows the results of BPM–DEM approach. We see with the increase of the mesh density, the calculated fracture aperture keeps increasing until converges at slightly higher values than the closed–form solution. This can be explained by the choices of penalty spring stiffness. By contrast, the results of CMEFM–FEM approach are quite close to the analytical solution. This may be attributed by: (*i*) the use of contact stress instead of contact force that somehow alleviates the sensitivity of penalty spring on the mesh sizes, (*ii*)

the advantages of combining FEM interpolation for continuum mechanics and contact calculation for discontinuum mechanics, and (*iii*) well–constrained penalty springs. Figure 8 shows similar yet magnified patterns of convergence of the maximum aperture calculated by these different approaches.

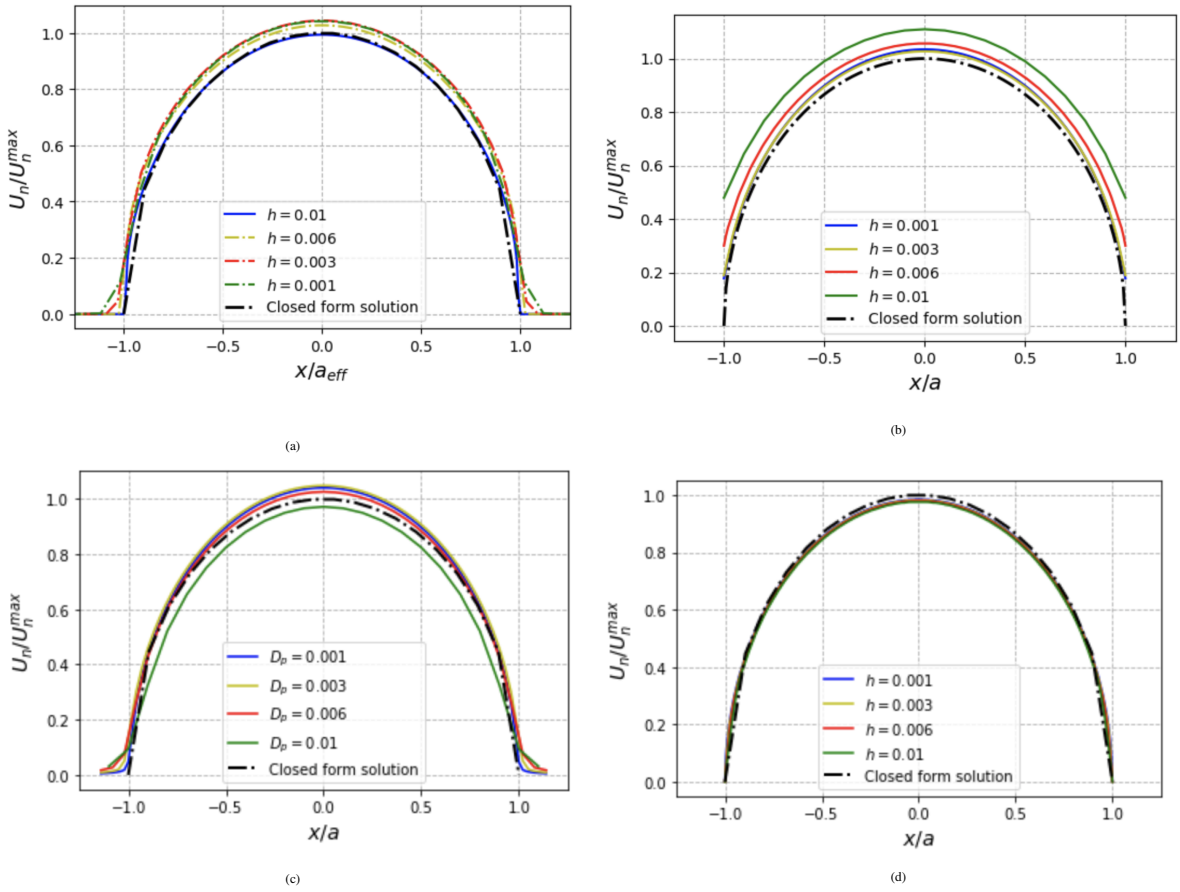

Figure 7: Fracture aperture profiles of (a) VPF–FEM, (b) hCA–FEM/xFEM, (c) BPM–DEM and (d) CMEFM–FEM with different mesh sizes compared against the analytical solution.

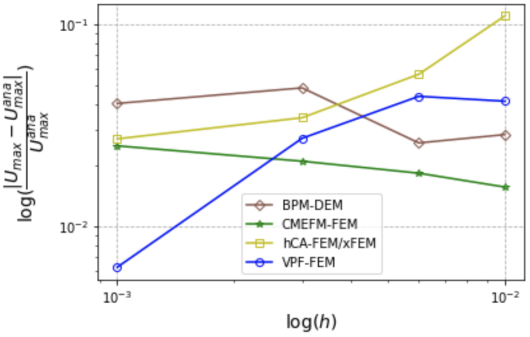

Figure 8: Convergence curve for the error of maximum aperture with different mesh sizes for benchmark 1.

3.5.2. Mesh alignment with inclined fracture in VPF–FEM

One of the advantages of the VPF–FEM is that we do not need to explicitly mesh the fracture and hence fractures do not have to propagate along pre-defined mesh elements. To see the effect of the alignment of mesh and fracture on fracture aperture, we repeated benchmark 4 with two different mesh inclinations (Figure 9) to see the impact of the alignment of mesh and fracture on fracture aperture . The fracture aperture is computed based on the line integral of the gradient of the phase field variable. [23, 79].

Figure 10 shows the aperture profiles from the VPF–FEM for the granite specimen with an inclined fracture. The aperture profile oscillates with the non-aligned mesh while the profile is smooth with the aligned (Figure 9a). The computation of aperture is inaccurate in the vicinity of the fracture tip because the crack's normal direction is improperly identified from the gradient of the phase field variable.

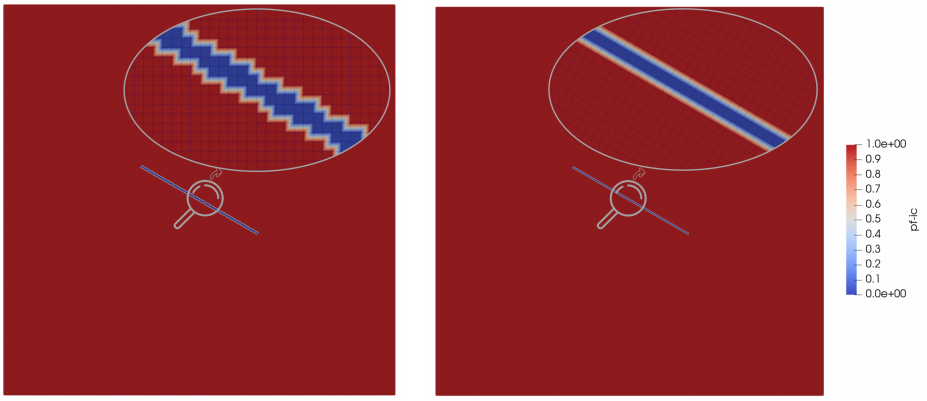

Figure 9: Initial phase field profile (a) not aligned mesh with inclined fracture and (b) aligned mesh with inclined fracture in VPF–FEM approach.

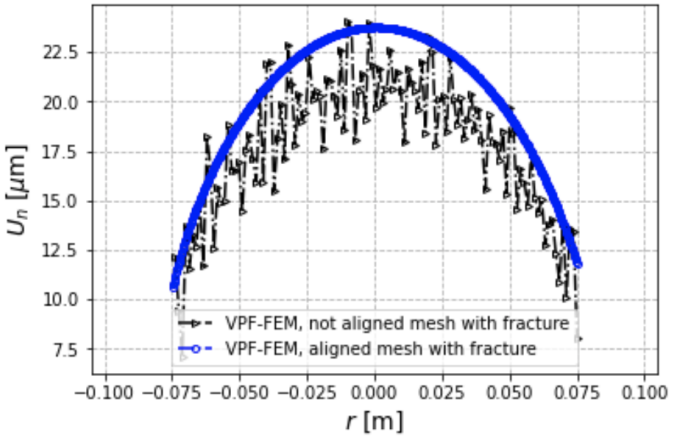

Figure 10: Aperture profiles for the Granite specimen with a plane inclined 30° fracture using VPF–FEM approach.

3.6. Domain size study

To investigate the effect of domain size and boundaries, we performed a series of examples with the same material and geometrical parameters, fracture size, and boundary conditions as benchmark 3 but with different domain sizes. We used four distinct computational domain sizes (m), $\Omega = [-0.125, 0.125] \times [-0.125, 0.125]$, $\Omega = [-0.25, 0.25] \times [-0.25, 0.25]$, $\Omega = [-0.5, 0.5] \times [-0.5, 0.5]$, and $\Omega = [-0.75, 0.75] \times [-0.75, 0.75]$ (Figure 11).

Figure 12 shows the results of using different domain sizes by different approaches. Despite the differences in the results which are similar to Figure 7, all the models show results converge when the domain size reaches or exceeds $\Omega = [-0.5, 0.5] \times [-0.5, 0.5]$. A notable difference between different teams is when the domain size $\Omega = [-0.25, 0.25] \times [-0.25, 0.25]$. Differently from other FEM and DEM approaches, the results calculated by IFDM–DEM show that when the domain size reaches $\Omega = [-0.25, 0.25] \times [-0.25, 0.25]$, the boundaries do not have an impact on the fracture aperture. Closer examination of the results of $\Omega = [-0.25, 0.25] \times [-0.25, 0.25]$, we found good agreement of the results by different approaches. Even though the width converges by increasing the domain size for each team, there is still a relatively significant difference between the calculated width in different team results. This difference could be due to (*i*) the lack of resolution for the region near the thin fracture for finite elements and (*ii*) the sensitivity to penalty springs.

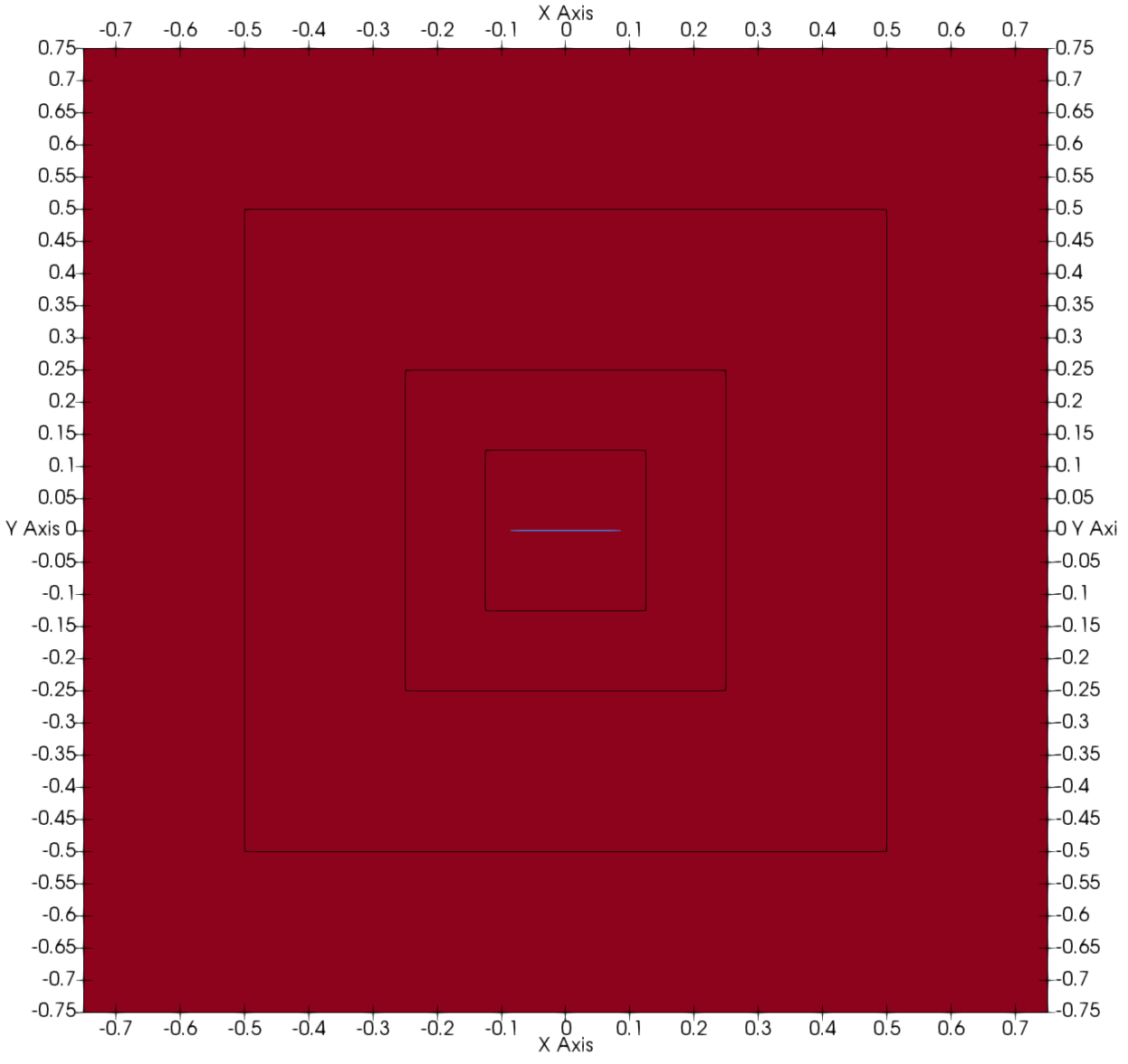

Figure 11: Domain size study for benchmark 3: $\Omega = [-0.125, 0.125] \times [-0.125, 0.125]$, $\Omega = [-0.25, 0.25] \times [-0.25, 0.25]$, $\Omega = [-0.5, 0.5] \times [-0.5, 0.5]$, and $\Omega = [-0.75, 0.75] \times [-0.75, 0.75]$. The unit of domain sizes is meter [m].

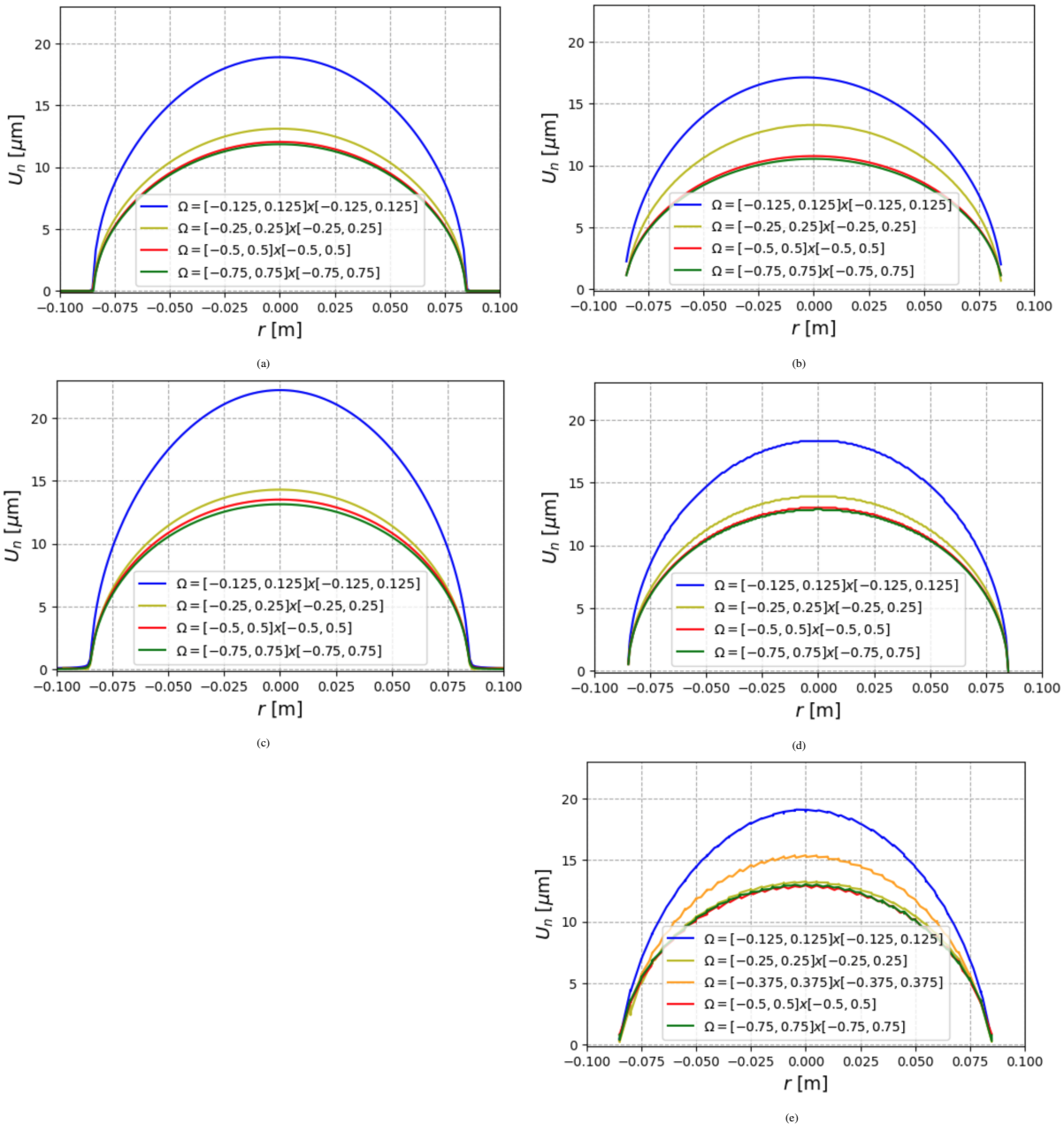

Figure 12: Aperture profiles of (a) VPF–FEM, (b) hCA–FEM/xFEM, (c) BPM–DEM, (d) CMEFM–FEM, and (e) IFDM–DEM for the Granite specimen with a plane horizontal fracture with different domain sizes.

4. Discussion

This section highlights the challenges and factors that impacted the numerical hydro–mechanical modeling of fracture processes. First, we briefly compare the benchmark results of the numerical methods used in this study. Next, each numerical approach's physical and numerical parameters are provided.

Table 3
Geometric representation of fractures in different software/codes by teams.

Team	Fractures mechanics		Fracture flow	
	Continuous	Discontinuous	Equi–dimensional	Reduced–dimensional
VPF–FEM	✓			✓
hCA–FEM/xFEM	✓		✓	
LIE–FEM		✓		✓
CMEFM–FEM		✓		✓
ETEL–FEM	✓			✓
GBM–DEM		✓		✓
BPM–DEM		✓		✓
IFDM–DEM		✓	✓	

4.1. Comparison of the fundamentals of different approaches

The differences in our approaches include numerical interpolation for the rock matrix, geometric representation of fractures in fluid flow and mechanics, and the coupling schemes between the fluid flow and mechanics. Additionally, meshing applied for fractures and the chosen parameters impact the computational results.

Geometric and hydro–mechanical representations of fractures The geometric representation of fractures can be categorized into continuous and discontinuous models for mechanics, and equi–dimensional and reduced–dimensional models for fluid flow. Equi–dimensional and reduced-dimensional representation refers to the dimension representing fractures compared with the dimension of the rock matrix. For example, if a fracture is represented with 2D elements in a 2D model, it is equi–dimensional. If a fracture is represented as 1D pipes/line segments, or with no additional degrees of freedom, the model is reduced–dimensional. Table 3 lists the different approaches of representing fractures in the software/codes that are used by different approaches.

For the benchmark problems, the equi–dimensional or reduced–dimensional fracture representation does not make a significant difference because the fluid pressure loss within the fracture is negligible. On the other hand, the mechanical representation of fractures influences the aperture or deformation of a fracture. The mesh needs sufficient resolution for the fracture to capture its deformation by various mechanical formulations.

The hCA–FEM/xFEM, ETEL–FEM, and VPF–FEM approaches tackle solid fracture in a continuum manner, whereas the LIE–FEM, CMEFM–FEM, GBM–DEM, BPM–DEM, and IFDM–DEM approaches treat it in a discontinuum manner. The VPF–FEM approach can describe a fracture with a slightly coarser mesh compared to conventional finite element methods because the fracture is indirectly represented by the phase field variable in a diffused manner.

In contrast, the other models represent fractures as explicit surfaces that can handle discontinuous displacement fields. The key functionalities are (*i*) to account for displacement jumps (open or slip); and (*ii*) to impose a unilateral constraint when the fracture is close (continuous displacement and discontinuous displacement gradient). The computation of slip adds another complexity because it involves not only the changes of contact states but also contact pairs. The contact algorithms used in this study (*e.g.* CMEFM–FEM) employ the penalty method to prevent over–penetration with small differences in the formulation. In CMEFM–FEM, contact stresses are calculated and integrated on segments, which is more accurate especially when element sizes are uneven. The fracture is connected to the solid rock by springs, in both shear and normal directions in ETEL–FEM approach. On the other hand, the contact model in DEM (GBM–DEM, BPM–DEM, IFDM–DEM) computes contact forces based on the contact areas.

Numerical interpolation The numerical approaches in this research can be classified as FEM and DEM–based approaches in general. FEM's key advantage is its ability to handle complicated geometry and smoothly varying properties and variables. The main disadvantage of FEM in fracture mechanics is that it needs refined elements around fracture tips, which may force re-meshing as fractures propagate [80]. Indeed, the mesh must conform to fractures as they propagate, increasing the computational cost. Several techniques to solve the re-meshing problem have been proposed (Universal Meshes [81], XFEM [80], Variational Phase-field [82]). On the other hand, DEM is computationally costly and struggles to achieve the same level of accuracy for continuous variables, but it would be much better at resolving contact loads.

Table 4
Physical and numerical parameters

Method	Static	Propagating
VPF–FEM	E, ν, ℓ	E, ν, ℓ, G_c
hCA–FEM/xFEM	E, ν, $\mathbf{k}$	–
LIE–FEM	E, ν, k_n, k_s	E, ν, k_n, k_s, G_c
CMEFM–FEM	E, ν, ρ, p_n	–
ETEL–FEM	E, ν, $\mathbf{k}$	–
GBM–DEM	E, ν, ρ, k_n, k_s	–
BPM–DEM	E, ν, ρ, k_n, k_s, μ_f	–
IFDM–DEM	E, ν, ρ, k_n, k_s, $\mathbf{k}$	–

Different numerical approaches interpolate the variables within the computational elements differently. In FEM–based approaches, linear or higher order interpolation is available to rigorously treat mechanical deformation. On the other hand, DEM approaches may suffer when the interpolation is 1D linear (spring connected elements), but these issues can be overcome with a well–constrained Poisson's ratio [83].

Coupling schemes In this study, the nonlinear hydro-mechanical problem is solved using staggered and monolithic coupling schemes. The coupled equations are solved simultaneously in a monolithic approach while the mechanical and fluid flow equations are solved separately in a staggered approach. As an example, Figure 13 illustrates the coupling schemes of the VPF–FEM (staggered scheme) and LIE–FEM (monolithic scheme).

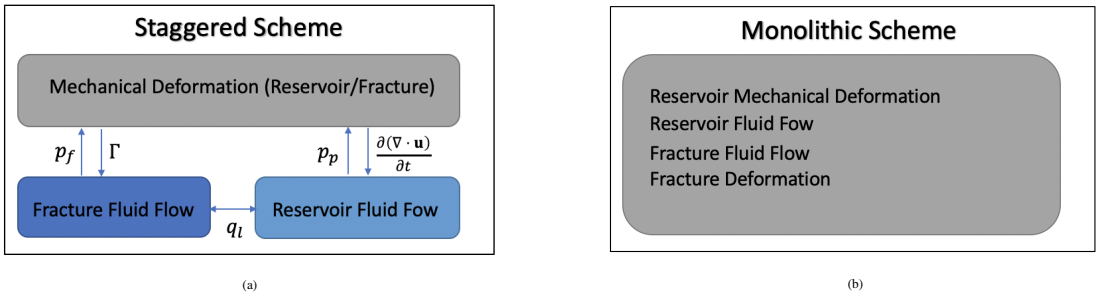

Figure 13: Coupling fluid flow and solid deformation algorithm in poroelastic media by (a) VPF–FEM and (b) LIE–FEM.

The staggered scheme has the advantage of allowing each set of governing equations to be solved by a different solver without the need for a computationally more competent unified solver. Furthermore, from the standpoint of computer programming, the governing equations in a staggered approach can be implemented within an existing mechanical or fluid flow computer code, providing more desired programming adaptability. However, because one of the processes (fluid flow or mechanics) is "frozen" while the other process is solved, it is known to pose some stability issues depending on which secondary variables (i.e. stress or strain) is chosen to be frozen and some stabilization parameters may be necessary [84, 85]. In this study, the staggered scheme is used in the following approaches: VPF–FEM, hCA–FEM/xFEM, GBM–DEM, BPM–DEM, IFDM–DEM.

In monolithic schemes, the mechanical and fluid flow equations are combined into a single problem and solved simultaneously with a single solver. The interface conditions, i.e., the continuity pressure defined by the monolithic problem, do not require sub-iterations to satisfy. As a result, monolithic schemes are often known as strongly coupled algorithms and numerically more stable [86]. The LIE–FEM, CMEFM–FEM, and ETEL–FEM approaches utilized the monolithic scheme for hydro-mechanical coupling.

4.2. Numerical/Physical parameters

Table 4 lists the numerical and physical parameters required for the different approaches. Even for seemingly simple physical problems such as our benchmark examples of the static crack aperture, each of the models requires a different set of parameters.

The key parameters for the discontinuous approaches are the stiffness of the penalty spring in both normal and shear directions (LIE–FEM, CMEFM–FEM, GBM–DEM, BPM–DEM, IFDM–DEM). VPF–FEM requires the regularization length parameter ℓ, which is a numerically parameter originally, but is regarded as a physical property in recent studies [87, 88].

5. Conclusions

This research is part of the DECOVALEX 2023 project, which aims to better understand geosystems via the lens of coupled thermo–hydro–mechanical–chemical processes. This study summarizes a comprehensive set of numerical methods in hydro-mechanical coupled fracture mechanics including continuous (VPF–FEM, hCA–FEM/xFEM, and ETEL–FEM) and discontinuous approaches (LIE–FEM, CMEFM–FEM, GBM–DEM, BPM–DEM, and IFDM–DEM).

We introduced a systematic benchmarking procedure to quantitatively evaluate and compare various numerical algorithms for hydro-mechanical coupled fracture mechanics. We deliberately devised benchmark problems as physically simple as possible while maintaining the important physics so that the problem set helps us examine each model's advantages and disadvantages in detail that could be masked behind the physical complexity in a more complex problem setting. Furthermore, our study demonstrates that even if an approach can match the closed-form solution under a benign condition (e.g., symmetric loading), its prediction can differ from other approaches under more realistic conditions.

We observed that all numerical approaches could reproduce the results of closed-form solutions in the benchmarks when suitably conditioned. On the other hand, the mesh study shows that different mesh resolutions are required to match closed-form solutions. Furthermore, the domain size study reveals that domain boundaries significantly influence the results, and the numerical methods are influenced differently in small domain sizes. This observation highlights the importance of investigating mesh and domain sizes in practical numerical modeling applications.

The qualitative comparisons between the numerical methods and closed-form solutions for static cracks show that all presented models can reproduce the maximum crack opening, but have difficulties near the crack tips.

Our simple benchmark settings show that each model requires a different number of parameters, even for simple physical problems, such as our static crack aperture benchmark examples. Using fewer parameters is in general more practical because it can prevent model overparameterization and ease experimental efforts.

The presented benchmark study will assist future experimental analysis within the DECOVALEX project. Future studies should expand a set of benchmark examples to more complex phenomena of fracture mechanics such as nucleation and complex fracture morphology and include validation against experiments.

Acknowledgements

DECOVALEX is an international research project comprising participants from industry, government, and academia, focusing on the development of understanding, models, and codes in complex coupled problems in subsurface geological and engineering applications; DECOVALEX-2023 is the current phase of the project. The authors appreciate and thank the DECOVALEX-2023 Funding Organisations Andra, BASE, BGE, BGR, CAS, CNSC, COVRA, US DOE, ENRESA, ENSI, JAEA, KAERI, NWMO, RWM, SÚRAO, SSM, and Taipower for their financial and technical support of the work described in this work. The statements made in the [paper/report] are, however, solely those of the authors and do not necessarily reflect those of the Funding Organisations.

The project teams want to acknowledge the funding of particular activities feeding into the international DECOVALEX community initiative:

- CAS: This research was financially supported by National Natural Science Foundation of China (Grant No. 52125903)
- KAERI: This research was supported by the Institute for Korea Spent Nuclear Fuel (iKSNF) and National Research Foundation of Korea (NRF) grant funded by the Korea government(Ministry of Science and ICT, MSIT) (2021M2E1A1085193).
- KIGAM: This research was supported by the Basic Research Project of the Korea Institute of Geoscience and Mineral Resources (GP2020-010) funded by the Ministry of Science and ICT, Korea.

- UFZ and TUBAF: We acknowledge funding from the German Federal Ministry of Education and Research (BMBF) for the GeomInt2 Project (grant number 03G0899D) for support in the development of the OGS phase-field method. Furthermore, the acknowledgments are extended to the European Joint Programme on Radioactive Waste Management (EURAD WP-DONUT and WP-GAS) within the Horizon 2020-Euratom program under grant agreement No 847593 (2019–2024).

References

[1] J.T. Birkholzer, C.-F. Tsang, A.E. Bond, J.A. Hudson, L. Jing, and O. Stephansson. 25 years of – scientific advances and lessons learned from an international research collaboration in coupled subsurface processes. *International Journal of Rock Mechanics and Mining Sciences*, 122, 2019.

[2] M.A. Biot. General theory of three-dimensional consolidation. *Journal of Applied Physics*, 12(2):155–164, 1941.

[3] B. Bourdin, G.A. Francfort, and J.-J. Marigo. Numerical experiments in revisited brittle fracture. *Journal of the Mechanics and Physics of Solids*, 48(4):797–826, 2000.

[4] Christian Miehe, Martina Hofacker, and Fabian Welschinger. A phase field model for rate-independent crack propagation: Robust algorithmic implementation based on operator splits. *Computer Methods in Applied Mechanics and Engineering*, 199(45):2765–2778, 2010.

[5] A Mesgarnejad, B Bourdin, and MM3340163 Khonsari. Validation simulations for the variational approach to fracture. *Computer Methods in Applied Mechanics and Engineering*, 290:420–437, 2015.

[6] M. Ambati, T. Gerasimov, and L. De Lorenzis. Phase-field modeling of ductile fracture. *Computational Mechanics*, 55(5):1017–1040, 2015.

[7] C. Kuhn, T. Noll, and R. Müller. On phase field modeling of ductile fracture. *GAMM Mitteilungen*, 39(1):35–54, 2016.

[8] Roberto Alessi, Jean-Jacques Marigo, Corrado Maurini, and Stefano Vidoli. Coupling damage and plasticity for a phase-field regularisation of brittle, cohesive and ductile fracture: One–dimensional examples. *International Journal of Mechanical Sciences*, 149:559–576, 2018.

[9] Bo Yin and Michael Kaliske. A ductile phase-field model based on degrading the fracture toughness: Theory and implementation at small strain. *Computer Methods in Applied Mechanics and Engineering*, 366:113068, 2020.

[10] B. Bourdin, C.J. Larsen, and C.L. Richardson. A time-discrete model for dynamic fracture based on crack regularization. *International Journal of Fracture*, 168(2):133–143, 2011.

[11] M.J. Borden, C.V. Verhoosel, M.A. Scott, T.J.R. Hughes, and C.M. Landis. A phase-field description of dynamic brittle fracture. *Computer Methods in Applied Mechanics and Engineering*, 217-220:77–95, 2012.

[12] Tianyi Li, Jean-Jacques Marigo, Daniel Guilbaud, and Serguei Potapov. Gradient damage modeling of brittle fracture in an explicit dynamics context. *International Journal for Numerical Methods in Engineering*, 108(11):1381–1405, 2016.

[13] Vinh Phu Nguyen and Jian-Ying Wu. Modeling dynamic fracture of solids with a phase-field regularized cohesive zone model. *Computer Methods in Applied Mechanics and Engineering*, 340:1000–1022, 2018.

[14] M. Seiler, P. Hantschke, A. Brosius, and M. Kästner. A numerically efficient phase-field model for fatigue fracture–1D analysis. *PAMM*, 18(1):e201800207, 2018.

[15] P. Carrara, M. Ambati, R. Alessi, and L. De Lorenzis. A framework to model the fatigue behavior of brittle materials based on a variational phase-field approach. *Computer Methods in Applied Mechanics and Engineering*, 361:112731, 2020.

[16] Keita Yoshioka, Mostafa Mollaali, and Olaf Kolditz. Variational phase-field fracture modeling with interfaces. *Computer Methods in Applied Mechanics and Engineering*, 384:113951, 2021.

[17] K Yoshioka, M Mollaali, G Mishaan, R Makhnenko, and F Parisio. Impact of grain and interface fracture surface energies on fracture propagation in granite. In *55th US Rock Mechanics/Geomechanics Symposium*. OnePetro, 2021.

[18] C. Maurini, B. Bourdin, G. Gauthier, and V. Lazarus. Crack patterns obtained by unidirectional drying of a colloidal suspension in a capillary tube: Experiments and numerical simulations using a two-dimensional variational approach. *International Journal of Fracture*, 184(1-2):75–91, 2013.

[19] Tuanny Cajuhi, L Sanavia, and Laura De Lorenzis. Phase-field modeling of fracture in variably saturated porous media. *Computational Mechanics*, 61(3):299–318, 2018.

[20] Emilio Martínez-Pañeda, Alireza Golahmar, and Christian F Niordson. A phase field formulation for hydrogen assisted cracking. *Computer Methods in Applied Mechanics and Engineering*, 342:742–761, 2018.

[21] Louis Schuler, Anastasia G Ilgen, and Pania Newell. Chemo-mechanical phase-field modeling of dissolution-assisted fracture. *Computer Methods in Applied Mechanics and Engineering*, 362:112838, 2020.

[22] Chuanjie Cui, Rujin Ma, and Emilio Martínez-Pañeda. A phase field formulation for dissolution-driven stress corrosion cracking. *Journal of the Mechanics and Physics of Solids*, 147:104254, 2021.

[23] B. Bourdin, C. Chukwudozie, and K. Yoshioka. A variational approach to the numerical simulation of hydraulic fracturing. In *SPE ATCE 2012*, 2012.

[24] M.F. Wheeler, T. Wick, and W Wollner. An augmented-Lagrangian method for the phase-field approach for pressurized fractures. *Computer Methods in Applied Mechanics and Engineering*, 271:69–85, 2014.

[25] Y. Heider and B. Markert. A phase-field modeling approach of hydraulic fracture in saturated porous media. *Mechanics Research Communications*, 80:38–46, 2017.

[26] D. Santillán, R. Juanes, and L. Cueto-Felgueroso. Phase field model of fluid-driven fracture in elastic media: Immersed-fracture formulation and validation with analytical solutions. *Journal of Geophysical Research: Solid Earth*, 122(4):2565–2589, 2017.

[27] Jinhyun Choo and WaiChing Sun. Cracking and damage from crystallization in pores: Coupled chemo–hydro–mechanics and phase–field modeling. *Computer Methods in Applied Mechanics and Engineering*, 335:347–379, 2018.

[28] Mostafa Mollaali, Vahid Ziaei-Rad, and Yongxing Shen. Numerical modeling of co2 fracturing by the phase field approach. *Journal of Natural Gas Science and Engineering*, 70:102905, 2019.

[29] Gilles A Francfort and J-J Marigo. Revisiting brittle fracture as an energy minimization problem. *Journal of the Mechanics and Physics of Solids*, 46(8):1319–1342, 1998.

[30] L. Ambrosio and V. M. Tortorelli. On the approximation of free discontinuity problems. *Boll. Un. Mat. Ital. B (7)*, 6(1):105–123, 1992.

[31] A. Braides. *Approximation of Free-Discontinuity Problems*. Number 1694 in Lecture Notes in Mathematics. Springer, 1998.

[32] C. Chukwudozie, B. Bourdin, and K. Yoshioka. A variational phase-field model for hydraulic fracturing in porous media. *Computer Methods in Applied Mechanics and Engineering*, 347:957–982, 2019.

[33] Lars Bilke, Bernd Flemisch, Thomas Kalbacher, Olaf Kolditz, Rainer Helmig, and Thomas Nagel. Development of open-source porous media simulators: principles and experiences. *Transport in porous media*, 130(1):337–361, 2019.

[34] Xia-Ting Feng, Peng-Zhi Pan, and Hui Zhou. Simulation of the rock microfracturing process under uniaxial compression using an elasto-plastic cellular automaton. *International Journal of Rock Mechanics and Mining Sciences*, 43(7):1091–1108, 2006.

[35] Peng-Zhi Pan, Jonny Rutqvist, Xia-Ting Feng, and Fei Yan. Modeling of caprock discontinuous fracturing during co2 injection into a deep brine aquifer. *International Journal of Greenhouse Gas Control*, 19:559–575, 2013.

[36] E. Papachristos, L. Scholtès, F.V. Donzé, and B. Chareyre. Intensity and volumetric characterizations of hydraulically driven fractures by hydro-mechanical simulations. *International Journal of Rock Mechanics and Mining Sciences*, 93:163–178, 2017.

[37] Peng-Zhi Pan, Xia-Ting Feng, and John A Hudson. Study of failure and scale effects in rocks under uniaxial compression using 3d cellular automata. *International Journal of Rock Mechanics and Mining Sciences*, 46(4):674–685, 2009.

[38] Pengzhi Pan, Xiating Feng, and Hui Zhou. Development and applications of the elasto-plastic cellular automaton. *Acta Mechanica Solida Sinica*, 25(2):126–143, 2012.

[39] Peng-Zhi Pan, Xia-Ting Feng, Hong Zheng, and Alexander Bond. An approach for simulating the thmc process in single novaculite fracture using epca. *Environmental Earth Sciences*, 75(15):1–16, 2016.

[40] Peng-Zhi Pan, Fei Yan, and Xia-Ting Feng. Modeling the cracking process of rocks from continuity to discontinuity using a cellular automaton. *Computers & Geosciences*, 42:87–99, 2012.

[41] Bernd Flemisch, Inga Berre, Wietse Boon, Alessio Fumagalli, Nicolas Schwenck, Anna Scotti, Ivar Stefansson, and Alexandru Tatomir. Benchmarks for single-phase flow in fractured porous media. *Advances in Water Resources*, 111:239–258, 2017.

[42] Gabriel Hattori, Jon Trevelyan, Charles E. Augarde, William M. Coombs, and Andrew C. Aplin. Numerical Simulation of Fracking in Shale Rocks: Current State and Future Approaches. *Archives of Computational Methods in Engineering*, 24(2):281–317, apr 2017.

[43] Satoshi Nishiyama, Yuzo Ohnishi, Hisao Ito, and Takao Yano. Mechanical and hydraulic behavior of a rock fracture under shear deformation. *Earth, Planets and Space*, 66(1):1–17, 2014.

[44] Brice Lecampion. An extended finite element method for hydraulic fracture problems. *Communications in Numerical Methods in Engineering*, 25:121–133, 2009.

[45] C. Vinci, J. Renner, and H. Steeb. A hybrid-dimensional approach for an efficient numerical modeling of the hydro-mechanics of fractures. *Water Resources Research*, 50(2):1616–1635, feb 2014.

[46] Inga Berre, Florian Doster, and Eirik Keilegavlen. Flow in Fractured Porous Media: A Review of Conceptual Models and Discretization Approaches. *Transport in Porous Media*, 130(1):215–236, oct 2019.

[47] Patrick Schmidt and Holger Steeb. Numerical aspects of hydro-mechanical coupling of fluid-filled fractures using hybrid-dimensional element formulations and non-conformal meshes. *GEM - International Journal on Geomathematics*, 10(1):14, dec 2019.

[48] Nori Watanabe, W Wang, J Taron, UJ Görke, and O Kolditz. Lower-dimensional interface elements with local enrichment: application to coupled hydro-mechanical problems in discretely fractured porous media. *International Journal for Numerical Methods in Engineering*, 90(8):1010–1034, 2012.

[49] K. Yoshioka, F. Parisio, D. Naumov, R. Lu, O. Kolditz, and T. Nagel. Comparative verification of discrete and smeared numerical approaches for the simulation of hydraulic fracturing. *GEM - International Journal on Geomathematics*, 10(1), 2019.

[50] T. Nagel, H. Shao, A.K. Singh, N. Watanabe, C. Roßkopf, M. Linder, A. Wörner, and O. Kolditz. Non–equilibrium thermo–chemical heat storage in porous media: Part 1 – Conceptual model. *Energy*, 60:254–270, 2013.

[51] COMSOL AB. Comsol multiphysics® v. 5.6. 2020.

[52] Thanh Son Nguyen. Progressive damage of a canadian granite in laboratory compression tests and underground excavations. *Minerals*, 11(1):10, 2021.

[53] E Ghazvinian, MS Diederichs, and R Quey. 3d random voronoi grain-based models for simulation of brittle rock damage and fabric-guided micro-fracturing. *Journal of Rock Mechanics and Geotechnical Engineering*, 6(6):506–521, 2014.

[54] Hengxing Lan, C Derek Martin, and Bo Hu. Effect of heterogeneity of brittle rock on micromechanical extensile behavior during compression loading. *Journal of Geophysical Research: Solid Earth*, 115(B1), 2010.

[55] Y Li, N Bahrani, et al. A numerical study on the failure process and strength of heterogeneous rocks and highly interlocked jointed pillars. In *54th US Rock Mechanics/Geomechanics Symposium*. American Rock Mechanics Association, 2020.

[56] Zhao Wang, Tiehang Wang, Saisai Wu, and Yanzhou Hao. Investigation of microcracking behaviors in brittle rock using polygonal grain-based distinct method. *International Journal for Numerical and Analytical Methods in Geomechanics*, pages 1–29, 2021.

[57] Paul Adams Witherspoon, Joseph SY Wang, K Iwai, and John E Gale. Validity of cubic law for fluid flow in a deformable rock fracture. *Water resources research*, 16(6):1016–1024, 1980.

[58] Itasca Consulting Group, Inc. Three–Dimensional Distinct Element Code (3DEC), Version 5.2. 2017.

[59] David O Potyondy and PA Cundall. A bonded-particle model for rock. *International journal of rock mechanics and mining sciences*, 41(8):1329–1364, 2004.

[60] James F Hazzard, R Paul Young, and Stephen J Oates. Numerical modeling of seismicity induced by fluid injection in a fractured reservoir. In *Mining and tunnel innovation and opportunity, Proceedings of the 5th North American rock mechanics symposium, Toronto, Canada*, pages

1023–1030. Citeseer, 2002.

[61] Jeoung Seok Yoon, Arno Zang, and Ove Stephansson. Numerical investigation on optimized stimulation of intact and naturally fractured deep geothermal reservoirs using hydro-mechanical coupled discrete particles joints model. *Geothermics*, 52:165–184, 2014.

[62] Jeoung Seok Yoon, Arno Zang, Ove Stephansson, Hannes Hofmann, and Günter Zimmermann. Discrete element modelling of hydraulic fracture propagation and dynamic interaction with natural fractures in hard rock. *Procedia Engineering*, 191:1023–1031, 2017.

[63] Harald Hökmark, Margareta Lönnqvist, and Billy Fälth. THM-issues in repository rock. thermal, mechanical, thermo-mechanical and hydro-mechanical evolution of the rock at the Forsmark and Laxemar sites. 2010.

[64] Itasca Consulting Group, Inc. PFC3D (Particle Flow Code in Three–dimensions), Version 4.0. *Minneapolis: ICG*, 3, 2008.

[65] K Pruess, C Oldenburg, and G Moridis. TOUGH2 user's guide, Version 2.1, LBNL–43134 (Revised). *Lawrence Berkeley National Laboratory, Berkeley, CA, USA*, 2012.

[66] Itasca Consulting Group, Inc. Three–Dimensional Distinct Element Code (3DEC), Version 7.0. 2020.

[67] S. Kwon, K.I. Kim, C. Lee, and J.S. Kim. Development of the three-dimensional discontinuum-based coupled hydro-mechanical simulator for modelling a deep geological repository. *In: Proceedings of 2021 Autumn Annual Conference of Korea Radioactive waste Society (KRS). Jeongseon, Korea*, 2021.

[68] I.N. Sneddon and M. Lowengrub. *Crack problems in the classical theory of elasticity*. The SIAM series in Applied Mathematics. John Wiley & Sons, 1969.

[69] Thomas Frühwirt, Daniel Pötschke, and Heinz Konietzky. Simulation of direct shear tests using a forces on fracture surfaces (ffs) approach. *Environmental Earth Sciences*, 80(8):1–10, 2021.

[70] I.N. Sneddon and M. Lowengrub. *Crack problems in the classical theory of elasticity*. John Wiley & Sons, 1969.

[71] E. Detournay. Mechanics of hydraulic fractures. *Annual Review of Fluid Mechanics*, 48:311–339, 2016.

[72] Lujun Ji, A. Settari, and R. B. Sullivan. A novel hydraulic fracturing model fully coupled with geomechanics and reservoir simulation. *SPE Journal*, 14(3):423–430, 2009.

[73] R H Dean and Joseph H Schmidt. Hydraulic-fracture predictions with a fully coupled geomechanical reservoir simulator. *SPE Journal*, 14(04):707–714, 2009.

[74] P Gupta and Carlos Armando Duarte. Simulation of non-planar three-dimensional hydraulic fracture propagation. *International Journal for Numerical and Analytical Methods in Geomechanics*, 38(13):1397–1430, 2014.

[75] S. Lee, M. F. Wheeler, and T. Wick. Pressure and fluid-driven fracture propagation in porous media using an adaptive finite element phase field model. *Computer Methods in Applied Mechanics and Engineering*, 312:509–541, 2016.

[76] T Gerasimov and L De Lorenzis. On penalization in variational phase-field models of brittle fracture. *Computer Methods in Applied Mechanics and Engineering*, 354:990–1026, 2019.

[77] A Mikelić, MF Wheeler, and T Wick. Phase-field modeling through iterative splitting of hydraulic fractures in a poroelastic medium. *GEM-International Journal on Geomathematics*, 10(1):2, 2019.

[78] A. A. Griffith. The phenomenon of rupture and flow in solids. *Phil. Trans. Roy. Soc. London*, 7(A 221):163, 1920.

[79] Keita Yoshioka, Dmitri Naumov, and Olaf Kolditz. On crack opening computation in variational phase-field models for fracture. *Computer Methods in Applied Mechanics and Engineering*, 369:113210, 2020.

[80] Ted Belytschko and Tom Black. Elastic crack growth in finite elements with minimal remeshing. *International journal for numerical methods in engineering*, 45(5):601–620, 1999.

[81] Ramsharan Rangarajan, Maurizio M Chiaramonte, Michael J Hunsweck, Yongxing Shen, and Adrian J Lew. Simulating curvilinear crack propagation in two dimensions with universal meshes. *International Journal for Numerical Methods in Engineering*, 102(3-4):632–670, 2015.

[82] Blaise Bourdin. Numerical implementation of the variational formulation for quasi-static brittle fracture. *Interfaces and free boundaries*, 9(3):411–430, 2007.

[83] Damien André, Jérémie Girardot, and Cédric Hubert. A novel dem approach for modeling brittle elastic media based on distinct lattice spring model. *Computer Methods in Applied Mechanics and Engineering*, 350:100–122, 2019.

[84] Jihoon Kim, Hamdi A. Tchelepi, and Ruben Juanes. Stability, Accuracy, and Efficiency of Sequential Methods for Coupled Flow and Geomechanics. *SPE Journal*, 16(02):249–262, 2011.

[85] Jihoon Kim, Hamdi A Tchelepi, and Ruben Juanes. Stability and convergence of sequential methods for coupled flow and geomechanics: Fixed-stress and fixed-strain splits. *Computer Methods in Applied Mechanics and Engineering*, 200(13-16):1591–1606, 2011.

[86] Yuri Bazilevs, Victor M Calo, Thomas JR Hughes, and Yongjie Zhang. Isogeometric fluid-structure interaction: theory, algorithms, and computations. *Computational mechanics*, 43(1):3–37, 2008.

[87] Erwan Tanné, Tianyi Li, Blaise Bourdin, J-J Marigo, and Corrado Maurini. Crack nucleation in variational phase-field models of brittle fracture. *Journal of the Mechanics and Physics of Solids*, 110:80–99, 2018.

[88] J.-Y. Wu. A unified phase-field theory for the mechanics of damage and quasi-brittle failure. *Journal of the Mechanics and Physics of Solids*, 103:72–99, 2017.

Highlights

Comparative verification of hydro-mechanical fracture behavior: Task G of international research project DECOVALEX–2023

Mostafa Mollaali,Olaf Kolditz,Mengsu Hu,Chan–Hee Park,Jung–Wook Park,Christopher McDermott,Neil Chittenden,Alex Bond,Jeoung Seok Yoon,Jian Zhou,Peng–Zhi Pan,Hejuan Liu,Wenbo Hou,Hongwu Lei,Liwei Zhang,Thomas Nagel,Markus Barsch,Wenqing Wang,Son Nguyen,Saeha Kwon,Changsoo Lee,Keita Yoshioka

- This research provides systematic benchmark tests to investigate various numerical approaches' numerical accuracy and parameterizations for hydro-mechanical coupled fracture mechanics.
- This study delves deeper into the numerical details of discretization effects (e.g., mesh sizes and orientation) and domain size for practical applications.
- The research compares several numerical approaches' parameterizations.